High Temperature Photocatalysis over Semiconductors

by

Thomas A. Westrich

A dissertation submitted in partial fulfillment
of the requirements for the degree of
Doctor of Philosophy
(Chemical Engineering)
in The University of Michigan
2012

Doctoral Committee:

Professor Johannes W. Schwank, Chair
Professor Massoud Kaviany
Professor Phillip Savage
Associate Professor Suljo Linic

To my family.

ACKNOWLEDGEMENTS

There are many people which I would like to acknowledge for their advice, help, and creativity. First and foremost, I would like to thank my advisor, Johannes Schwank. Johannes was always inspired me to try new things and push the limits of experimental design. I would also like to thank my committee members for their advice and review. In particular, I would like to recognize the significant contribution Massoud Kaviany has made to the progression of this thesis. Without his knowledge of heat transfer physics and encouragement, I would have been stymied long ago.

To the graduate students of the Michigan Chemical Engineering Department, I am deeply happy to have made so many lifelong friends and collegues.

I would like to thank my wife, Meghan, for her encouragment and support. She was a brilliant source of inspiration whenever I was at an impasse. I would also like to thank my brother, Bradford, my parents, Henry and Mary Westrich, and my grandparents, Thomas Parke and Gloria Grace Myers for all of their support, encouragement and patience.

TABLE OF CONTENTS

LIST OF FIGURES

Figure

LIST OF TABLES

Table

LIST OF APPENDICES

Appendix

ABSTRACT

High Temperature Photocatalysis over Semiconductors

by

Thomas A. Westrich

Chair: Johannes W. Schwank

Due in large part to in prevalence of solar energy, increasing demand of energy production (from all sources), and the uncertain future of petroleum energy feedstocks, solar energy harvesting and other photochemical systems will play a major role in the developing energy market. This dissertation focuses on a novel photochemical reaction process: high temperature photocatalysis (i.e., photocatalysis conducted above ambient temperatures, T $\geq$ 100°C).

The overarching hypothesis of this process is that photo-generated charge carriers are able to constructively participate in thermo-catalytic chemical reactions, thereby increasing catalytic rates at one temperature, or maintaining catalytic rates at lower temperatures. The photocatalytic oxidation of carbon deposits in an operational hydrocarbon reformer is one envisioned application of high temperature photocatalysis. Carbon build-up during hydrocarbon reforming results in catalyst deactivation, in the worst cases, this was shown to happen in a period of minutes with a liquid hydrocarbon. In the presence of steam, oxygen, and above-ambient temperatures, carbonaceous deposits were photocatalytically oxidized over very long periods ($t \geq$ 24 hours).

This initial experiment exemplified the necessity of a fundamental assessment of high temperature photocatalytic activity. Fundamental understanding of the mechanisms that affect photocatalytic activity as a function of temperatures was achieved using an ethylene photocatalytic oxidation probe reaction. Maximum ethylene photocatalytic oxidation rates were observed between 100 °C and 200 °C; the maximum photocatalytic rates were approximately a factor of 2 larger than photocatalytic rates at ambient temperatures. The loss of photocatalytic activity at temperatures above 200 °C is due to a non-radiative multi-phonon recombination mechanism. Further, it was shown that the fundamental rate of recombination (as a function of temperature) can be effectively modeled as a temperature-dependent quantum efficiency term, and is directly driven by bulk photocatalyst crystal parameters: maximum phonon energy and the number of phonons allowed per unit cell. This analysis extends to multiple photocatalysts and can explain experimental observations of photocatalytic oxidation rates with varied reactant concentrations. Lastly, this dissertation applies this knowledge to a thermo-catalytic reaction (CO-oxidation) using a Au/TiO_2 catalyst. The combined photo/thermo-catalytic reaction showed a 10-25% increase in CO conversion during a temperature programmed reaction experiment.

CHAPTER I

Introduction

1.1 A Brief Introduction on Photocatalysis

Photocatalysis has seen a surge of recent interest due, in large part, to rising energy costs and ecological awareness (see Figure 1.1). Photocatalysts are simply semiconducting materials that have a distinct energy gap between electron orbital states that are occupied (valence) and unoccupied (conducting). A simplified orbital diagram for TiO_2 was produced by Umebayashi, and can be seen in Figure 1.2.

Metals, for instance, have a continuous population of electrons between the valence and conducting bands; thus, metals are able to conduct electricity very easily. On the other hand, insulating materials have a very large gap between the valence and conduction bands, thereby making them very effective barriers to electricity flow. Somewhere between these two extremes lie photocatalysts, which use visible and ultraviolet (UV) light to excite electrons from the valence band to the conduction band. The excited electron leaves an effective electron vacancy in the valence band, which is named a hole. The electron/hole pair is called an exciton.

The generation of the exciton is determined by the photocatalyst band gap and the wavelength (or energy) of incident light. Once created, the exciton pair has a strong tendency to recombine, which produces heat. In fact, one of the biggest limitations of photocatalysts is their high recombination rate; high recombination of excitons

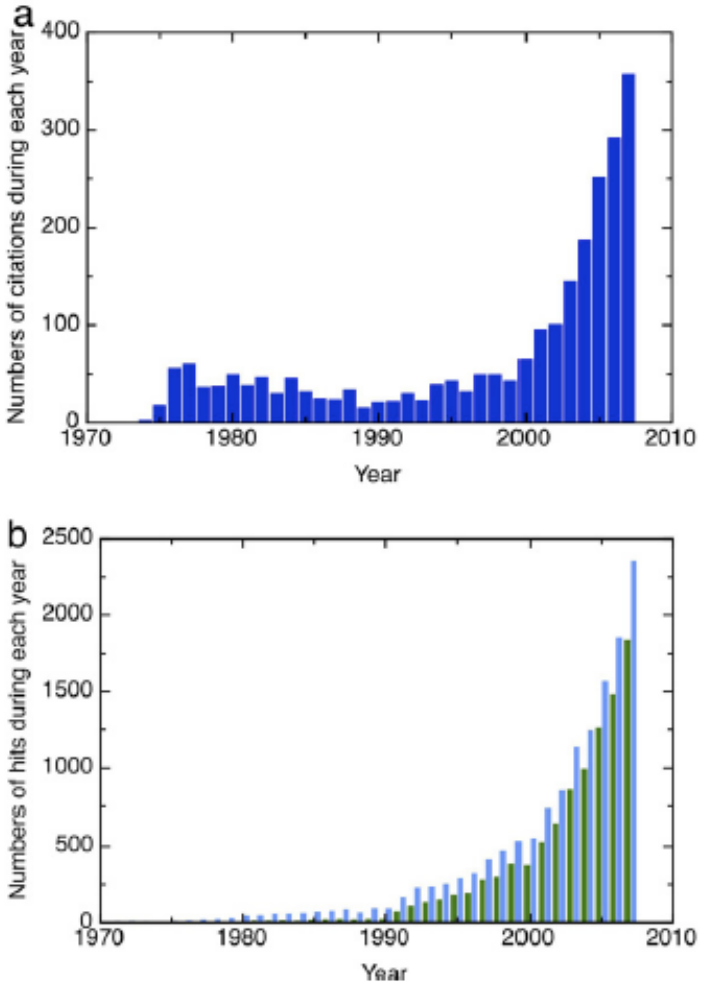

Figure 1.1: Number of citations of a single 1972 Nature paper on electrochemical splitting of water (A), and the number of Web of Science search results for photocatalyst (B); image courtesy of [3].

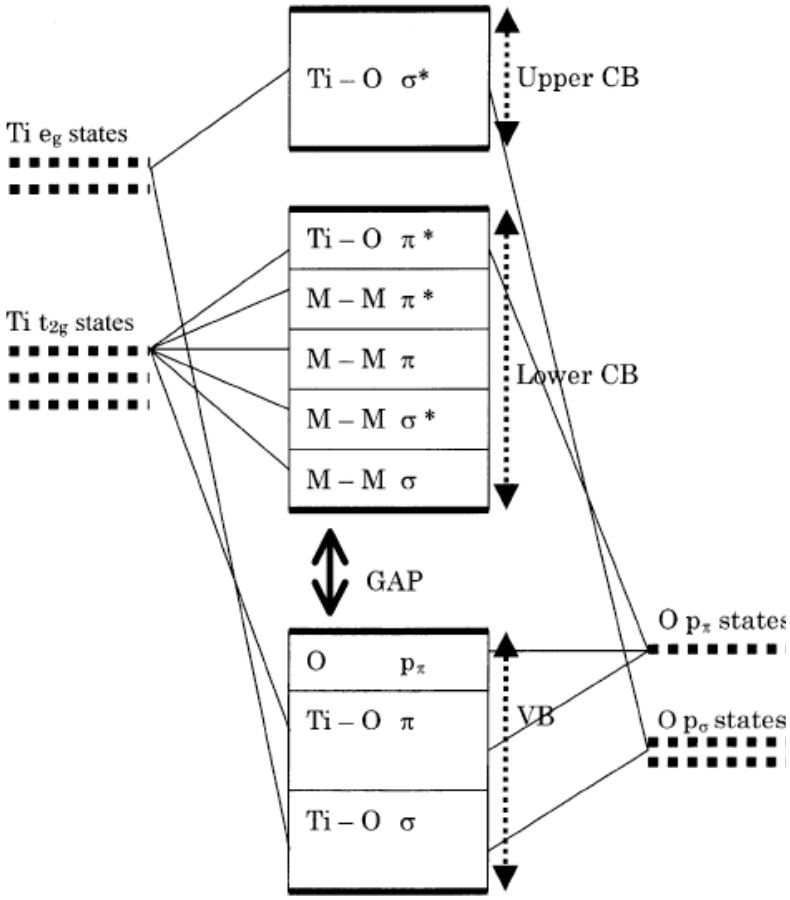

Figure 1.2: Molecular orbital diagram of TiO_2, courtesy of Umebayashi, et. al. [4].

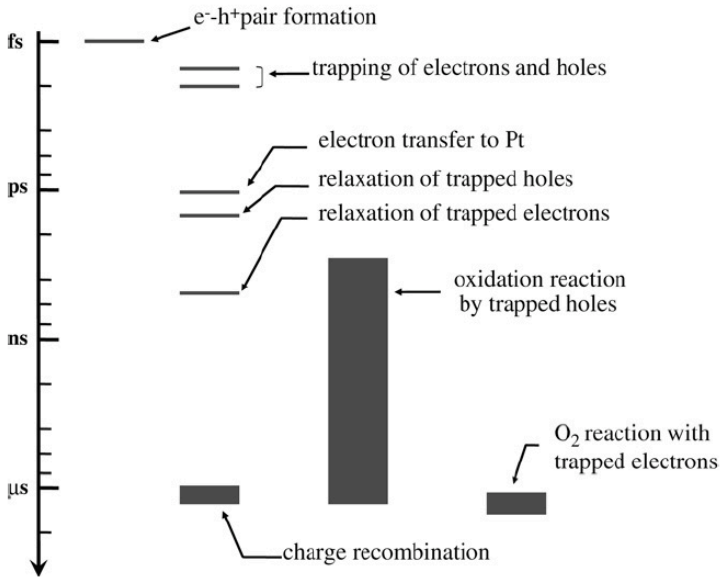

Figure 1.3: Relative rates of exciton transfer and trapping mechanisms. Image courtesy of [3].

results in less available electrons and holes for other chemistry [7]. The relative time constants associated with exciton migration can be seen in Figure 1.3.

In order to generate the exciton pair, the photocatalyst must be illuminated with light of a particular energy, or minimum wavelength. This means that the generation of high-energy excitons (i.e., excitons in titania crystals) is energetically difficult with incident solar radiation. Titania, at room temperature and in its anatase phase, has a band gap of 3.2eV. A photon of equivalent energy has a wavelength of 373nm. If the incident solar spectrum is used to generate this electron on titania, then only about 3-5% of insolation can be used a relatively low percentage. If the photocatalyst has a lower band gap, then more of the incident solar spectrum might be used, however, the produced exciton would have a lower energy. Figure 1.4 illustrates this: the intensity (power) of the incident solar radiation increases with increasing wavelength (direction of decreasing band gap). In Figure 1.4, power corresponds to the integrated area under the intensity curves. For reference, the relative energy levels of water oxidation and reduction half reactions are shown in Figure 1.5, along with the conduction and

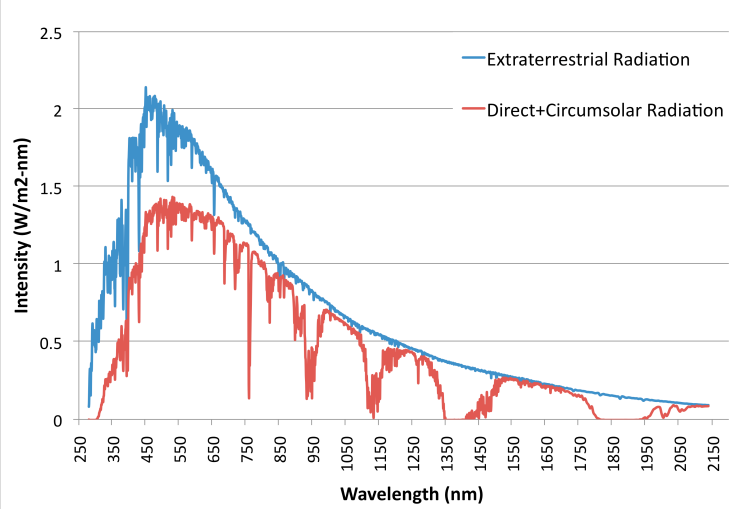

Figure 1.4: Incident Solar radiation on the Earth. Extraterrestrial radiation data is collected outside of Earth's atmosphere. Direct+Circumsolar radiation encompasses the radiation (as seen from the surface of the Earth) from the 5 degree disk, centered on the sun. Data provided by the National Renewable Energy Laboratory's Reference Solar Spectral Irradiance database.

valence bands for TiO_2.

1.2 Possibilities and Applications of Photothermal Catalysis

The catalytic processing of lower value chemicals into higher value chemicals typically requires elevated catalyst temperatures to activate reactant molecules. Industrially relevant examples include ammonia synthesis (wherein temperatures of approximately 200−400°C are needed to dissociatively adsorb nitrogen) and methane steam reforming (which requires temperatures in excess of 600°C to activate methane). In both of these examples, thermal energy is used to overcome large activation barriers for the rate limiting dissociative adsorption steps. On the electronic level, dissociation occurs due to the probabilistic population of electrons in the adsorbate's anti-bonding orbitals − this probability increases with increasing temperatures. In much the same way, electrochemical or photochemical processes use energetic electrons (which interact with surface adsorbates) to facilitate chemical reactions. However, what is

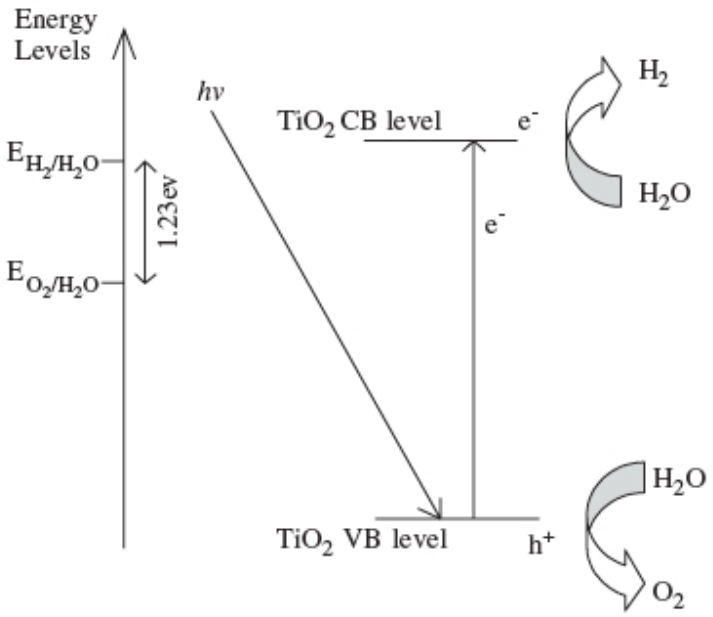

Figure 1.5: Energy diagram of valence and conduction bands of TiO_2, as well as the reduction and oxidation potentials for water. Image courtesy of Ni, et al. [5].

unknown is the additive effects of these alternate approaches to catalysis. For instance, is it possible to utilize photocatalytically generated electrons to offset the thermal energy needed to activate an adsorbate, such as nitrogen or methane, and produce high-value chemicals (ammonia or hydrogen) at lower temperatures, or with lower materials or operational costs?

Many photocatalytic reactions are operated under ambient conditions, particularly in an aqueous medium, as is the case in water splitting reactions. One substantial segment of missing information is the effect of temperature on photocatalytic activity. Very few authors have investigated photocatalysis at temperatures in excess of 100°C. Therefore, in order to proceed with the investigation of photo-thermal catalytic production of industrially relevant, or energetically useful chemical production, the basic investigation of elevated temperature photocatalytic activity should be accomplished. To illustrate the usefulness of such photo-thermal processes, consider the example of

carbon deposition during liquid hydrocarbon reforming, and its potential mitigation and catalyst activation through a photo-thermal process.

Hydrogen and syngas (gaseous mixture of H_2 and CO) is currently produced via the reforming of hydrocarbons specifically methane, but liquid hydrocarbon reforming is also possible. All of these reforming reactions are run at elevated temperatures over transition metal catalysts such as platinum or nickel. Due to the large costs associated with large-scale reforming over noble metal catalysts, cheaper transition metal catalysts are typically used (i.e. nickel). Unfortunately, nickel is prone to excessive carbon formation and subsequent deactivation during hydrocarbon reforming. Some techniques can be used to alleviate much of this carbon formation, such as introduction of excess oxidants (steam and oxygen, in the steam reforming and partial oxidation reactions, respectively); however, this does not completely eliminate the problem of coking.

In order to remove deposited carbon, oxidation is required. Oxidation is problematic for two reasons: downtime of the reforming reactor leads to inefficient operation, and high oxidation temperatures sinter catalysts or otherwise detrimentally affect catalyst performance. Photocatalysis offers a new approach for carbon mitigation. Lee and Choi [8] showed that soot, as deposited by a hexane flame on a TiO_2 substrate, could be photocatalytically removed at room temperature. Mills, et al. presented similar results from the photo-oxidation of butane-derived soot on a TiO_2 substrate [9]. In both cases, room temperature photocatalytic oxidation of carbon species was accomplished.

The second chapter of this thesis has been published in Applied Catalysis A: General and is focused on the detrimental effects of carbon deposition on current state-of-the-art hydrocarbon reforming catalysts [1]. Of particular interest are the temperatures required to produce hydrogen, and the rates of carbon deposition, which accompany hydrogen production. It is with this knowledge that we might be able to

further investigate the requirements of a catalyst and reactor which may be used to minimize carbon deposits via photocatalytic oxidation.

In the third chapter of this thesis, I will outline and discuss the requirements of a photocatalytic reactor operating at elevated temperatures. In order to observe relevant data, it is also important to ensure that the photocatalytic reactions operate within a chemically relevant kinetic reaction regime. The developed photocatalytic reactor and control scheme were then used in the remaining work to conduct photocatalytic reaction measurements for different reactions, from photocatalytic oxidation of carbon deposits to the photocatalytic oxidation of hazardous compounds.

In the fourth chapter, the photocatalytic oxidation of carbon is evaluated, specifically as an alternative carbon mitigation strategy during reforming reactions. Although this oxidation strategy could be employed as a carbon mitigation strategy during hydrocarbon reforming, the work discussed in chapter four is conducted at a lower temperature, in order to observe carbon oxidation rates in the absence of thermally-driven oxidation reactions.

The fifth chapter of this thesis has been published in the Journal of Physical Chemistry C, and is focused on the limitations of photocatalysts operating at reforming temperatures [2]. In this work, the photocatalytic oxidation of ethylene at temperatures ranging from room temperature to 500°C shows the inherent limitations of operating photocatalysts at such high temperatures. However, with the knowledge gained from this work, it is possible to evaluate individual photocatalysts for their ability to conduct chemistries at elevated temperatures based on fundamental photocatalyst crystal parameters.

In the sixth chapter, this photocatalyst evaluation model is extended to different reaction mechanisms, such as ethylene oxidation in a dry air stream and ethylene oxidation over ZnO rather than TiO_2. From these three probe reactions, we can determine the limits of this analysis technique, and possibly think about alternate,

and potentially, more applicable, photocatalytic systems, such as the photocatalytic oxidation of carbon monoxide. Carbon monoxide oxidation is critically important to polymer electrolyte membrane fuel cells, as it acts as a poison for their hydrogen-activation catalysts (notably, platinum).

The overarching theme of this thesis is to set the fundamental building blocks of future efforts in high temperature photocatalysis, but specifically for photo-thermal processes. Such processes are envisioned to replace energy intensive, inefficient, large-carbon-footprint chemical processes with a solar-thermal and solar-photocatalytic process with a somewhat smaller carbon-footprint. It is by these incremental improvements that photothermal catalytic research will advance, and possibly affect positive, energy-efficient changes in the way we conduct industrial chemical production.

CHAPTER II

Carbon Deposition over Ni-based Hydrocarbon Reforming Catalysts [1]

2.1 Abstract

Catalytic decomposition of hydrocarbons is a major contributor to carbon formation during hydrocarbon reforming. This work investigates the effects of temperature and hydrocarbon decomposition intermediates on carbon deposition during catalytic isooctane decomposition over ceria-zirconia supported nickel. The carbon deposition rate and hydrocarbon concentrations were monitored in real-time via thermogravimetry and FT-IR spectroscopy. Carbon-deposited catalysts were characterized by temperature-programmed oxidation (TPO) and scanning electron microscopy (SEM). Carbon deposition rate, morphology, and quantity were strongly dependent on decomposition temperature (T); three distinct decomposition temperature regimes were identified, i.e. $T \leq 575$ °C, 575 °C $< T <$ 725 °C, and $T \geq 725$ °C. Gaussian deconvolution of TPO data and carefully designed oxidation experiments indicated the presence of different types of carbon: coating, filamentous, and pyrolytic carbon. Catalytic and homogeneous decomposition of isooctane, propene, and methane suggest that smaller hydrocarbon fragments, typically formed during reforming of large hydrocarbon molecules, play an important role in carbon deposition. Specif-

ically, low-temperature decomposition of isooctane into olefins, such as propene or isobutene, leads to the formation of both coating and filamentous carbon deposits. At high temperatures, decomposition of acetylene and methane leads to the formation of significant quantities of coating and pyrolytic carbon deposits in addition to filamentous deposits.

2.2 Introduction

Reforming and decomposition of liquid hydrocarbons (LHCs) to H_2-rich gas are active areas of research [10, 11]; such H_2-production techniques have also attracted interest in transportation applications [12, 13]. Nickel (Ni) is a promising alternative to precious metal reforming catalysts due to its lower cost, and because it activates the carbon-hydrogen bond readily. Recently, extensive efforts have been devoted to Ni-catalyzed reforming of LHCs [10], including steam reforming (SR) [10, 13–16], partial oxidation (POX) [10, 13, 17, 18], and autothermal reforming (ATR) [10, 13, 19–25]. Nickel-based solid oxide fuel cell (SOFC) anodes have also received attention for their use as direct internal-reforming systems [26–30], particularly for automotive auxiliary power units (APU) [31]. Fuel flexibility is desirable for such applications; nickel anode catalysts can operate with fuels such as H_2, CO, CH_4 [26, 28, 29], and LHCs [32].

A key challenge to operating Ni-catalyzed hydrocarbon reformers is avoiding carbon deposition [10, 12, 13, 27–29, 32, 33] while sustaining high H_2 yield and stable anode performance [34]. It is well known that Ni-based catalysts are prone to deactivation due to carbon deposition [35, 36]. There is an extensive body of literature addressing carbon nucleation, growth, and morphologies during reforming of methane or light hydrocarbons [10, 36–41]. Various strategies for carbon mitigation have been developed, including modifications of catalyst formulations [10, 13, 38, 42, 43], mainly via stabilizing [44] or reducing Ni particle size [38, 40, 43, 45], using bimetallic catalysts [16, 25, 46, 47] to promote surface properties of Ni catalysts [38, 43, 48]

or forming surface Ni-metal alloys [14, 15, 30, 40, 49–51], modifying the support [10, 44, 45, 52–54], pre-reforming [55], and others [42, 56]. Among the formulation modifications of Ni-containing catalysts or SOFC anodes, promotion by ceria [29, 43, 53] and surface Au-Ni alloying [57] appeared to be the most effective as these methods led to remarkable carbon-tolerance and enhanced performance in direct reforming of methane in SOFCs [29, 33]. As a result, a nearly carbon-deposition-free operation could be achieved even with low steam to methane ratios [53, 57]. Studies indicated that the role of ceria [58] in mitigating carbon formation is attributed to the redox properties of ceria [54, 59] promoting oxygen mobility [58, 60, 61] or, alternatively, is attributed to the strong interaction between ceria and active Ni [58, 62, 63]. The design of reforming catalysts with increased stability can be challenging, due to the numerous reactions and intermediate products involved. The reforming pathway, e.g. steam reforming, is generally described in literature as Eq. (2.1).

$$C_m H_{(2m+2)} + mH_2 \rightarrow mCO + (2m+1)H_2 \tag{2.1}$$

As the detailed mechanistic aspects of carbon deposition from LHCs are poorly understood, carbon mitigation strategies similar to those used in methane reforming have extensively been adopted [10, 13–18, 21, 22, 24, 30, 64–67]. Unlike methane reforming [41], the in-situ study of carbon formation and growth during reforming of LHCs is a very difficult task. Carbon deposits present on post-reforming catalysts [68–70] represent accumulated carbon species, which result from the balance between carbon deposition, gasification, and oxidation [43]. This is particularly true when ceria is used as support or promoter as it can accelerate steam gasification [62, 71]. Furthermore, previous studies indicated that significant amounts of light hydrocarbons (carbon numbers less than 5) are formed during reforming of LHCs [23, 66], and under partial oxidation conditions [72]. These light hydrocarbons may play a signifi-

cant role in final hydrogen production [23, 73], and carbon deposition [21]. However, to our best knowledge, the relationship between smaller hydrocarbon intermediates and carbon deposition during reforming of LHCs is still poorly understood.

Thus this work investigated the effect of decomposition temperature and the role of decomposition fragments of isooctane on carbon deposition over ceria-zirconia supported Ni catalysts.

2.3 Experimental

2.3.1 Catalyst Preparation

The catalyst support material, ceria-zirconia mixed oxide ($Ce_{0.75}Zr_{0.25}O_2$, denoted CZO), was prepared via the coprecipitation method by titrating 2M ammonium hydroxide (Aldrich) aqueous solution into a mixed aqueous solution of $Ce(NO_3)_2$ (Aldrich) and $ZrOCl_2$ (Aldrich) under constant stirring [68]. The suspension was stirred overnight, aged at room temperature, and then recovered by filtration and washed thoroughly with deionized water. The filter cake was then dried in an oven at 120 °C overnight and calcined at 600 °C in air for 2 h. Nickel loading was achieved via incipient wetness impregnation of the calcined support material by a nickel nitrate aqueous solution. The samples were then further calcined at 650 °C in air for 2 h to obtain NiO supported on CZO (NiO/CZO), followed by reduction in flowing H_2 at 850 °C, as described later in the decomposition section.

2.3.2 Catalyst Characterization

BET surface area measurements were carried out by a single point method on a Quantachrome CHEMBET-3000. Ni dispersion was measured on a Micromeritics ASAP 2020 instrument by performing both CO and H_2 chemisorption at 35 °C. Ni dispersion was calculated from the difference between total and weak adsorption

volumes by assuming an adsorption stoichiometry of one CO molecule or one H atom corresponding to one exposed nickel surface atom. The unreduced 10 wt.% Ni/CZO catalyst (NiO/CZO) had a BET surface area of 37 ± 0.5 m^2 g^{-1}. After H_2 reduction at 850 °C, the BET surface area decreased to 25 ± 0.5 m^2 g^{-1}, indicating some sintering of either CZO support or nickel metal itself. Chemisorption data for the 10 wt.% Ni/CZO sample reduced at 600 °C showed a nickel dispersion of 1.6 ± 0.02 % and nickel active surface area of 1.05 ± 0.03 m^2 g^{-1}_{cat}, corresponding to an average nickel particle size of 63 ± 2 nm.

2.3.3 Isooctane Decomposition

2.3.3.1 Reactor System Configuration

Isooctane decomposition reactions over Ni/CZO were carried out in the quartz furnace tube of a thermogravimetric analyzer (TA Q500). The composition of the effluent gas stream was monitored by a Nicolet 380 IR spectrometer. The predominant advantage of the combination of TGA and IR used in this work is the on-line acquisition of catalyst mass data and the corresponding concentration of reactant and products throughout the experiment. From this information, it is possible to identify the hydrocarbon(s) responsible for carbon deposition via interpretation of the IR spectra. The IR band assignments of isooctane and its decomposition products were determined using published NIST data and the spectral libraries that were included with the IR spectrometer. The representative vibrational peaks for each hydrocarbon are shown in Table 2.1. The integration of these peaks was used to represent the relative concentration of each compound.

Isooctane (99% reagent grade, Sigma-Aldrich) was introduced to the TGA reactor using a liquid/gas saturator at room temperature. Analysis of post-saturator isooctane concentration indicated that the isooctane concentration in the carrier gas flow could be effectively controlled by the carrier gas flow rate, while keeping all other

Table 2.1: Infrared band assignment of the species during isooctane decomposition.

Compound	Centered IR Band (cm^{-1})	Characteristic vibration
Isooctane	1215/1176	Tert−butyl $C-C$ skeletal
Isobutene	888	$C-H$ out−of−plane bend for vinylidene $C=CH_2$
Propylene	912	$C-H$ out−of−plane bend for vinyl $CH=CH_2$
Ethylene	1888	CH_2 wag for combination of (v_7+v_8)
Acetylene	730	Alkyne $C-H$ bend
Methane	1303	$C-H$ bend
Benzene	730	$C-H$ out−of−plane bend for aromatic ring

saturator variables constant (saturator temperature and isooctane liquid level). The isooctane concentration was also confirmed using diffusion calculations for isooctane vapor-phase transport in nitrogen bubbles. The isooctane concentration was constant for all experiments, due to the constant TGA balance and sample gas flow rates.

2.3.3.2 Homogeneous Isooctane Decomposition

Homogeneous isooctane pyrolysis was performed by flowing isooctane (4.1vol% in nitrogen) through the blank TGA reactor as the furnace cooled from 850 °C to 450 °C at a rate of 5 °C min^{-1} in the absence of a catalyst. As the reactor cooled, IR spectra of the effluent gases were continuously acquired.

2.3.3.3 Catalytic Isooctane Decomposition

Preliminary catalytic isooctane decomposition experiments were first conducted using catalysts with a wide range of Ni loading (2-10 wt.% Ni) in order to identify a metal loading that produced concentrations of decomposition products large enough to allow detection with the IR spectrometer. Low Ni loadings, such as 2-5 wt.% produced relatively small quantities of decomposition products. All data presented in this work were collected over a 10 wt.% Ni/CZO catalyst as this catalyst generated

sufficient integrated intensities of the relevant IR peaks even at low decomposition temperatures.

Prior to catalytic decomposition experiments, NiO/CZO was reduced in situ to Ni/CZO. Typically, 10 mg of NiO/CZO was loaded into the TGA reactor, and the entire system was purged with pure N2 flow for 30 minutes. The gas flow was then changed to 5% H_2/N_2 for 15 minutes before the TGA furnace was heated to 120 °C. After the furnace was held at 120 °C for 15 minutes to remove physically adsorbed water, the sample was then ramped to 850 °C at 10 °C min^{-1} and held at 850 °C for 90 minutes. After this 90-minute hold in H_2/N_2, the catalyst was considered fully reduced and stabilized. Then the Ni/CZO catalyst was cooled to the desired decomposition temperature: 425, 500, 575, 650, 725, or 800 °C. The gas flow was then switched to pure N_2 for a 5 min period to flush residual H_2.

After 5 minutes of IR data collection under pure N_2 flow at the desired decomposition temperature, the isooctane stream (4.1 vol.%) was introduced to the reactor. After 60 minutes of decomposition at constant temperature, the gas flow was switched to pure N_2 flow to prevent further hydrocarbon decomposition and preserve the carbon morphology and structure achieved during the 60-minute decomposition. The furnace was then immediately cooled to 120 °C under the protection of pure N_2 flow. In addition to isooctane decomposition over Ni-loaded CZO, the decomposition of isooctane over the blank support (CZO) was investigated using this procedure to distinguish the contribution of Ni and CZO on carbon deposition and morphology.

In order to witness transient differences between the IR spectra of catalytic and homogeneous isooctane decomposition species, additional homogeneous decomposition experiments were conducted. In these experiments, time-dependant, isothermal isooctane decomposition was conducted in the absence of a catalyst at 500 °C and 650 °C, using a procedure identical to the catalytic isooctane decomposition procedure, described above. IR data from each homogeneous and catalytic experiment

can be directly compared to determine the catalysts influence on the effluent product spectrum. Specifically, the IR data of the catalytic experiment may be subtracted from the IR data of the homogeneous experiment for each effluent product. The subtracted data reveals negative IR data (representing the catalytic production of an effluent product) and positive IR data (representing the catalytic consumption of said product). Given this information for all IR-visible species, it is clear which hydrocarbons are consumed or produced due to the presence of a catalyst during an experiment.

2.3.3.4 Propene and Methane Decomposition

The decomposition of propene and methane, which represent primary and secondary isooctane decomposition products, was performed to investigate their independent effects on carbon deposition at certain temperatures. These tests used identical procedures to the isooctane decomposition experiments; however, the hydrocarbons were fed into the reactor via a mixed gas standard. The concentration of methane used was 10 vol% in N_2, and the propene concentration was 3.0 vol% in N_2. The homogeneous decomposition experiments were conducted at 500, 600, 700, and 800 °C for 60 minutes. The catalytic decompositions of methane and propene over Ni/CZO were conducted at 500 °C and 650 °C. For comparison, propene decomposition over blank CZO support was carried out over a similar temperature range.

2.3.4 Carbon Characterization

The carbon-deposited catalysts were removed from the TGA reactor, finely ground, and divided into batches. Typically, one of these batches was subjected to temperature-programmed oxidation (TPO) using TGA to ensure consistency between identical decomposition experiments. TPO experiments were carried out using a temperature ramp of 10 °C min^{-1} to 800 °C in air. The presence of carbon on the sample was

confirmed by the identification of CO_2 IR spectra during TPO. Deposited carbon morphology was determined by a FEI Nova Nanolab scanning electron microscope (SEM). The SEM was operated at 10-15 kV and 0.14-0.58 nA, depending on the surface charging of the sample. The specimens were prepared by loading the ground sample onto an Al-Mg alloy holder. Sputter-coating of gold or carbon on the SEM samples was unnecessary, as the samples were already highly conductive.

2.4 Results

2.4.1 Homogeneous Decomposition

2.4.1.1 Homogeneous Isooctane Decomposition

The integrated IR bands of isooctane and its decomposition products versus reaction temperature are shown in Fig. 2.1; the integrated IR bands reflect the relative concentration of each individual product. Therefore, these results can be used to interpret the decomposition products of isooctane over a range of temperatures. For instance, isooctane conversion was negligible below 450 °C as its integrated IR value is at a maximum, and complete conversion was observed above 715 °C.

At 500 °C, very low homogeneous isooctane conversion ($< 3\%$) was observed. Detectable decomposition products included isobutene, propene, and methane. When the furnace temperature reached 615 °C, additional cracking products, such as ethylene and acetylene, were observed. At higher temperatures ($\sim$ 650 °C), isooctane was increasingly converted (60%). Larger integrated IR values were recorded for isobutene, propene, and methane, indicating their presence in higher concentrations. The maximum isobutene concentration was observed at 675 °C, while propene reached its maximum concentration at 715 °C. These two temperatures corresponded to isooctane conversions of 80% and 100%, respectively. Based on calibration of the IR band intensity using a propene/N_2 standard, the propene concentration corresponding to

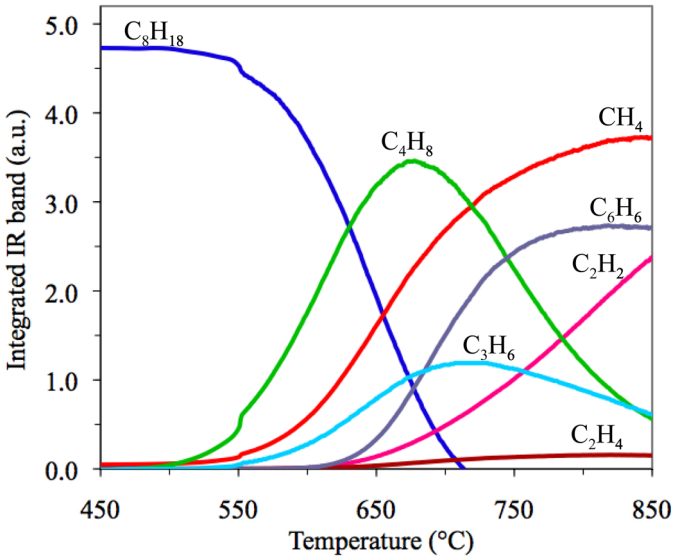

Figure 2.1: Integrated IR bands for isooctane and its homogeneous decomposition products versus temperature.

the integrated IR value at 715 °C was 3.7 vol.%. Isobutene and propene could be further decomposed above 715 °C, as observed by their decreasing concentration. The maximum ethylene concentration was 2.1 vol.%, which occurred at a furnace temperature of 820 °C. The maximum methane concentration (observed at 850 °C) corresponded to 5.5 vol.%, as determined by calibration with a standard gas. Benzene was unexpectedly observed at temperatures above 615 °C; the maximum benzene concentration was observed near 820 °C.

2.4.1.2 Homogeneous Propene Decomposition

In an effort to prove that acetylene, benzene and ethylene were formed from further decomposition and polymerization of primary isooctane decomposition products, a 2.4 vol.% propene (balance N_2) flow was introduced into the blank TGA reactor in the temperature range of 500 °C to 800 °C. IR analysis of the effluent gases showed no IR spectra of decomposition products at reactor T $\leq$ 600 °C. At 700 °C, very low (0.5%) conversion of propene was detected, accompanied by very weak IR spectra of

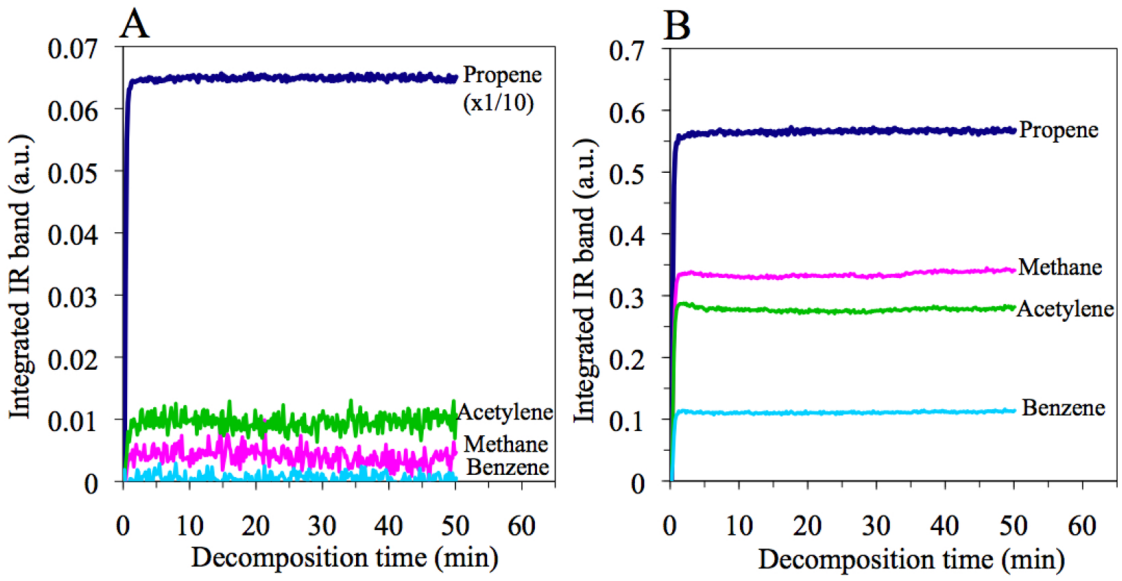

Figure 2.2: Integrated IR band profiles versus deposition time during homogeneous propene decomposition at 700 °C (A) and 800 °C (B).

methane, acetylene, and benzene, indicating homogeneous decomposition of propene as shown in Fig. 2.2a. Moreover, when the temperature was further increased to 800 °C, conversion of propene increased (13%) and very strong IR spectra of methane, acetylene, and benzene were observed, as shown in Fig. 2.2b. However, the ethylene band was very weak; the integrated intensity was negligible (close to baseline). These experiments are consistent with the isooctane decomposition results (shown in Fig. 2.1), confirming that methane, acetylene, benzene, and ethylene could be secondary products in the decomposition of isooctane. After propene decomposition at 800 °C, a film of carbon was noticed on the internal surfaces of the TGA reactor (ceramic and metal surfaces alike). It is reasonable to assume that the pyrolysis of the secondary decomposition products contribute to pyrolytic carbon deposition at elevated temperatures during the decomposition of isooctane.

2.4.2 Catalytic Isooctane Decomposition

2.4.2.1 IR Product Analysis

Fig. 2.3 shows the derivative weight (i.e. derivative thermogravimetric, or DTG) curves of the catalyst and the difference of integrated IR bands between catalytic and homogeneous isooctane decomposition species. The subtraction of catalytic product IR data from homogeneous product IR data reveals information about the role of Ni/CZO catalysts on hydrocarbon consumption and production. The inset of Fig. 2.3 illustrates the calculation of the isooctane consumption feature during decomposition at 500 °C. The difference in IR values for isooctane in the homogeneous and catalytic experiments results in a positive value, indicating that the catalyst leads to additional isooctane decomposition beyond that observed during homogeneous decomposition.

As shown in Fig. 2.3, the presence of a catalyst at 500 °C results in the enhanced decomposition of isooctane and the net production of methane and solid carbon (evidenced by DTG curve) during the initial 15 minutes of decomposition. As the decomposition progressed, the isooctane consumption and methane production went through a maximum, and then gradually returned to zero. This result shows that the active surface sites responsible for catalytic decomposition of isooctane became deactivated with increasing time. Traces of isobutene and acetylene were observed at this temperature; however, there was no significant difference in IR values of isobutene or acetylene between homogeneous and catalytic decomposition experiments. Much more pronounced differences in IR data of intermediate species were observed when isooctane decomposition was carried out at elevated temperatures. Many of the species homogeneously formed at 650 °C are catalytically consumed during the first 10 minutes of decomposition, resulting in the net production of methane and solid carbon. IR data from the 800 °C isooctane decomposition are not presented in Fig. 2.3 because data acquired at this temperature represents

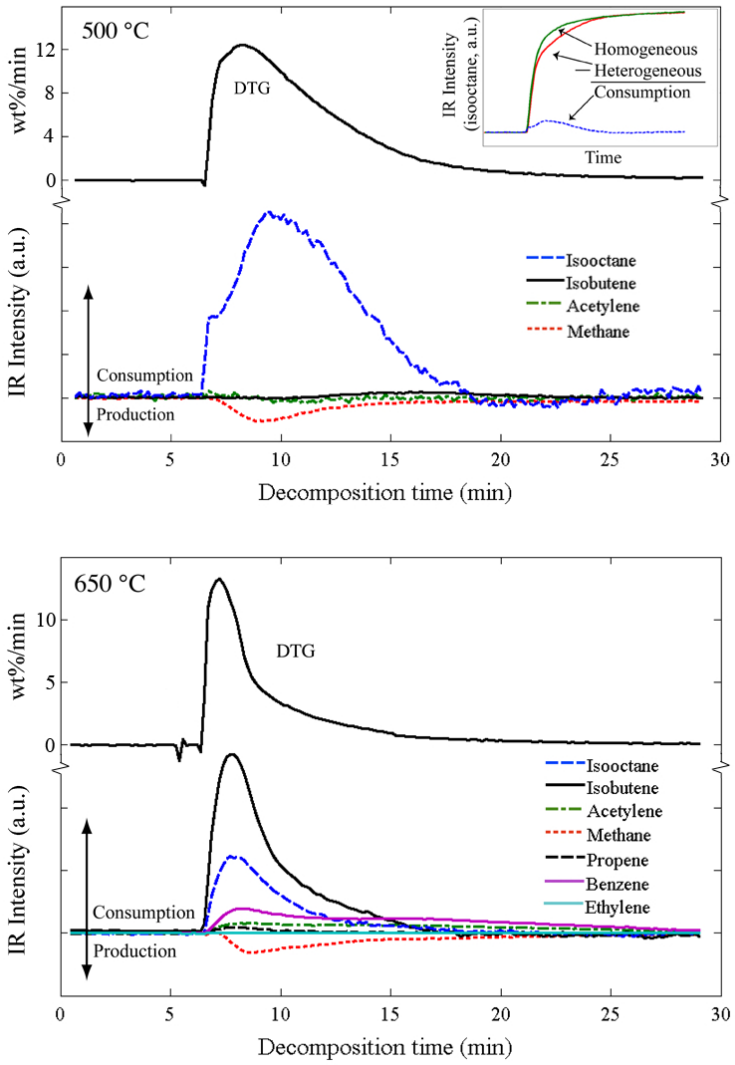

Figure 2.3: Carbon formation rate (DTG) over catalyst and the difference of integrated IR bands for observed products during isooctane decomposition at 500 °C (top) and 650 °C (bottom). The inset illustrates the calculation of the isooctane consumption feature during decomposition at 500 °C.

the decomposition of a mixture of secondary isooctane decomposition products and this work is primarily concerned with carbon deposition derived from isooctane and its primary decomposition products.

2.4.2.2 Carbon Deposition

In all catalytic decomposition experiments, the reduced catalyst weight increased sharply within the initial few minutes of exposure to isooctane due to carbon deposition; the catalyst then experienced a much longer period of significantly lower weight gain. The overall extent and the rate of carbon deposition depended primarily on the isooctane decomposition temperature. Catalytic decomposition of isooctane was performed at temperatures of 425, 500, 575, 650, 725, and 800 °C. Fig. 2.4 shows the TGA data from each 60-minute isooctane decomposition at typical temperatures, i.e. 500, 650, and 800 °C. It should be noted that the results presented in Fig. 2.4 reflect carbon deposition on nickel only, as the contribution of carbon deposited on the CZO support was subtracted. The corresponding carbon formation rate (i.e. DTG curve) as a function of decomposition time is illustrated in Fig. 2.3 for the 500 °C and 650 °C experiments.

At low decomposition temperatures, e.g. 500 °C, the catalyst experienced an 86 wt.% mass increase due to carbon formation over a 60-minute period. DTG data show that the maximum rate of carbon formation occurred 2.8 minutes after the introduction of isooctane. Carbon growth continued for 13 minutes after the introduction of isooctane. Of the carbon deposited, 90% was deposited within this initial 13-minute period. At moderate decomposition temperatures (650 °C), only 46 wt.% carbon was deposited over the course of 60-minutes. The carbon formation rate reached a maximum 1.9 minutes after the introduction of isooctane and became negligible 12 minutes after isooctane introduction. Again, most of this carbon (90%) was deposited in the initial 12 minutes. The maximum carbon deposition rates for

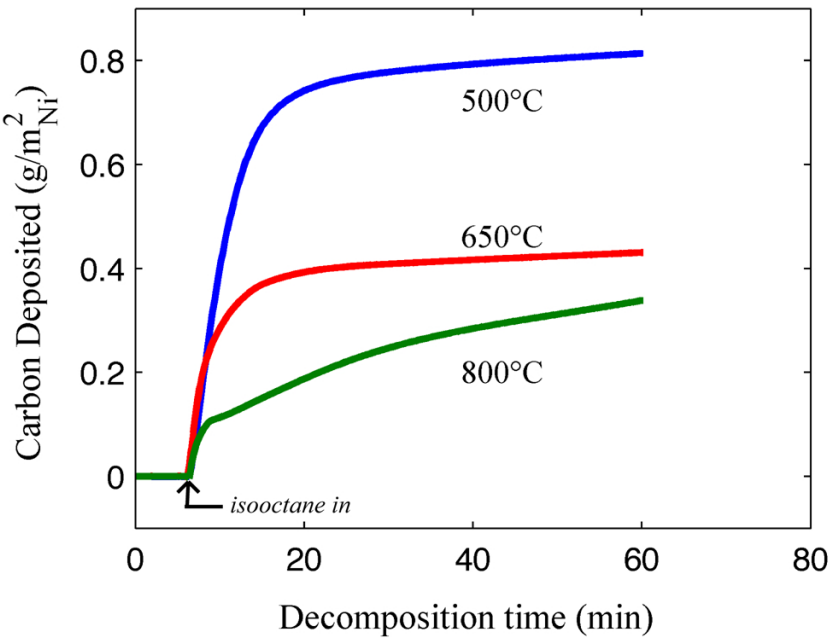

Figure 2.4: Deposited carbon mass on the catalyst during isooctane decomposition at different temperatures.

the 500 and 650°C decomposition experiments are very similar: 12.45 wt% min^{-1} and 13.29 wt% min^{-1}, respectively. The full width at half maximum (FWHM) of the 650 C DTG curve (Fig.3) was 110 seconds, in contrast to the 500 °C DTG FWHM of 325 seconds, indicating that the period of rapid carbon deposition lasted three times longer at 500 °C than at 650 °C. At high decomposition temperatures, e.g. 800 °C (Fig. 4), carbon deposition was markedly different from depositions at lower temperatures. The initial period of high carbon deposition rate lasted only 2 minutes, rather than 10-13 minutes, as in lower temperature decomposition experiments. A relatively small weight gain (11 wt.%) was observed at the end of this initial 2-minute period. It is important to note that at 800 °C, most if not all of the isooctane may have homogeneously decomposed prior to reaching the catalyst surface. This would then imply that the carbon build-up would be due to decomposition of intermediate species such as methane, acetylene, and others. This could explain the very different

slope of the 800 °C weight gain curve after the initial 2 minute period. Isooctane decomposition over the support (CZO) shows mass gains of 0.2, 1.4, and 14.7wt% at the end of the 60-minute decomposition.

The morphologies of typical Ni/CZO catalysts post isooctane decomposition at temperatures of 500, 650, and 800 °C were characterized by SEM. Fig. 2.5 shows the micrographs of these samples. Obviously, the decomposition temperature plays a major role in determining the morphology and size of filamentous carbon. Based on the analysis of SEM images, it is possible to measure and compile filament diameter distributions for each decomposition temperature. Isooctane decomposition at 500 °C led to the deposition of carbon filaments that averaged 16 nm in diameter, but ranged from 12 to 65 nm in diameter and hundreds of nanometers in length. The mean filament diameter of carbon filaments formed from isooctane decomposition at 650 °C was 21 nm: similar to the mean filament diameter of carbon formed during low-temperature decompositions. In addition, many filaments appeared to have their surface decorated with small, insulating particles, presumably catalyst (Ni/CZO) particles. In contrast, relatively large carbon filaments were formed at 800 °C, with mean diameter of about 80 nm. SEM was also used to characterize the morphology of carbon deposits from the isooctane decomposition over blank CZO. No filamentous carbon was observed on CZO after isooctane decomposition at 500 °C, 650 °C, or 800 °C (SEM micrographs are not shown). The deposited carbon on CZO appears to uniformly coat the surface and worked as conductor when acquiring SEM images [68]. This carbon is most likely a deposited as a result of pyrolysis mechanisms.

2.4.2.3 Oxidation Characterization of Carbon Deposits

Previous work for isooctane ATR over Ni/CZO catalysts defined two types of deposited carbon, i.e. coating and filamentous carbon, according to morphological characterization, TPO and XPS [68]. Results from that work suggested that TPO

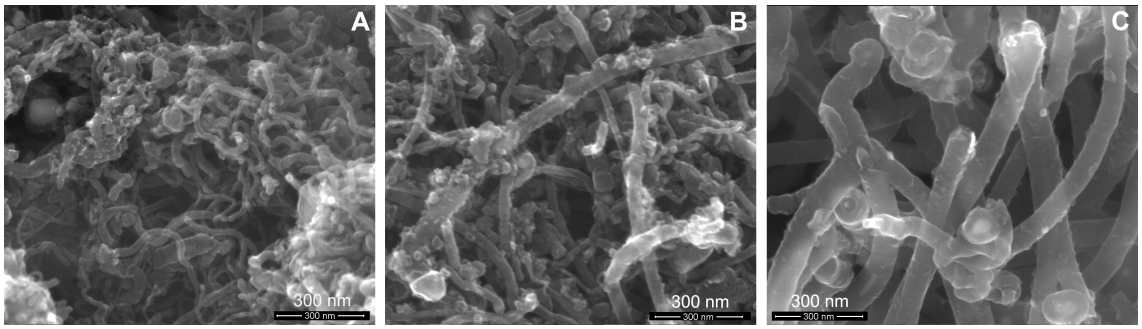

Figure 2.5: Scanning electron micrographs of catalysts from 60-minute isooctane decomposition at 500 °C (A), 650 °C (B), and 800 °C (C).

could be used to estimate carbonaceous morphologies present in a sample via the identification of oxidation peaks. Therefore, TPO was carried out as an efficient estimation method in the speciation of carbon formed from isooctane catalytic decomposition. Fig. 2.6 shows derivative TPO (dTPO) curves of carbon formed during the 60-minute isooctane decomposition over Ni/CZO at different decomposition temperatures. Based on the analysis of TPO results, three typical temperature regions for carbon deposition could be identified, i.e. $T \leq 575$ °C; 575 °C $< T <$ 725 °C; and $T \geq 725$ °C. Varying the isooctane decomposition temperature led to large differences in dTPO features. At low decomposition temperatures ($T \leq 575$ °C), the deposited carbon oxidized in one main feature near 550 °C. Further, on-line IR analysis of gaseous products during TPO experiments showed a lack of water or hydrocarbon species present in the effluent gas, indicating the absence of CHx species in carbon-deposited sample. At moderate decomposition temperatures (575 °C $< T <$ 725 °C), the deposited carbon oxidized in two large features and one small feature ranging in peak oxidation temperature from 290 °C to 620 °C. At very high decomposition temperatures ($T \geq 725$ °C), there appeared to be two very large oxidation features at 400 °C and 600 °C.

Gaussian fitting of dTPO peaks was conducted to thoroughly analyze the observed oxidation features. This data analysis revealed the presence of 3-4 oxidation

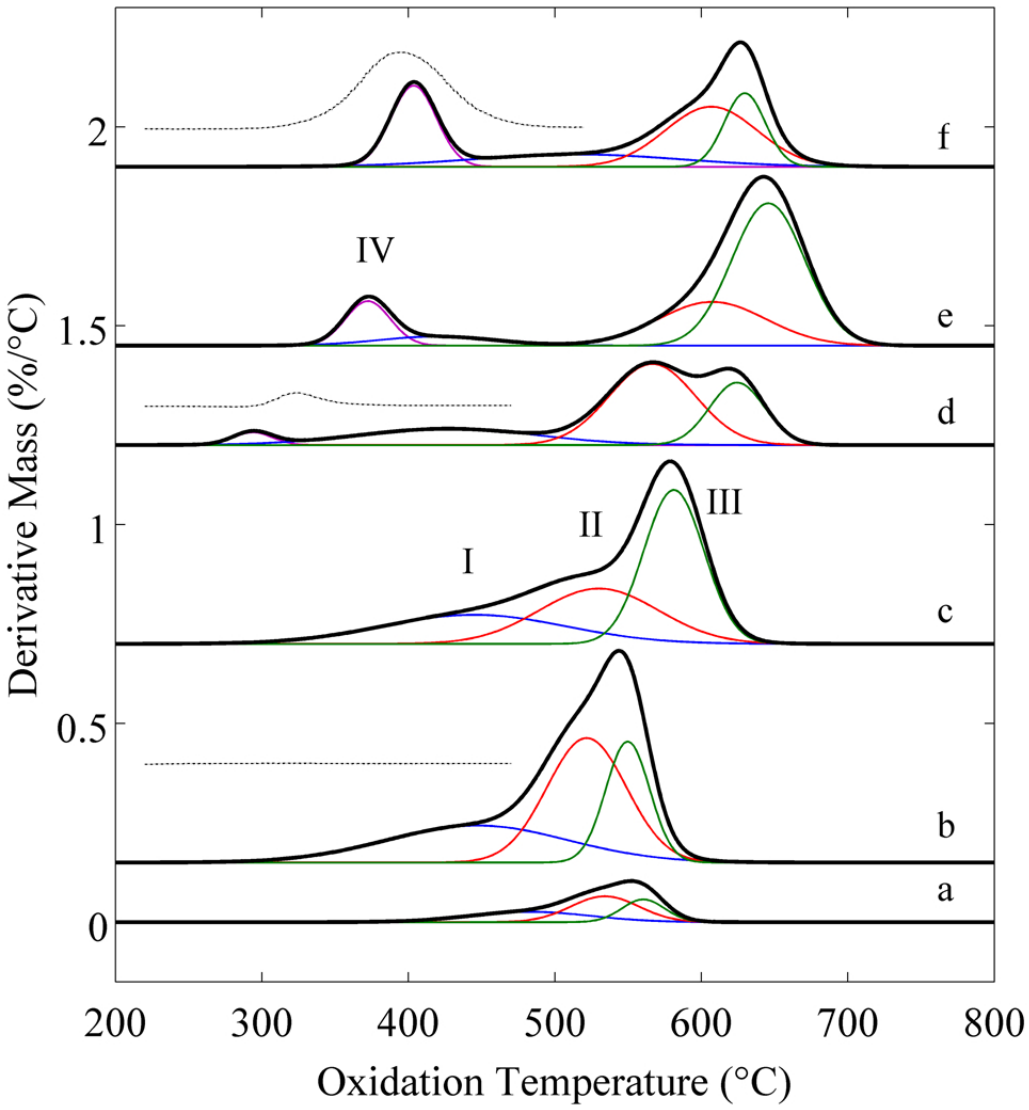

Figure 2.6: Derivative TPO curves of carbon deposited catalysts obtained after isooctane decomposition at 425 °C (a), 500 °C (b), 575 °C (c), 650 °C (d), 725 °C (e), and 800 °C (f) for 60 minutes. Each TPO trace was deconvoluted into 3-4 Gaussian peaks to aide in identification of the carbon morphologies present in each sample. The dotted curves, which represent TPO of bare CZO samples post isooctane decomposition, are located directly above TPO curves for Ni/CZO catalysts obtained at the same relative decomposition temperature.

Table 2.2: Gaussian deconvolution analysis for TPO features of various carbon deposits.

	Peak of Oxidation Temperature (deposited carbon, wt%)			
Decomposition Temperature	I	II	III	IV
425°C	483.2°C (2.9)	534.1°C (3.6)	560.3°C (2.5)	N/A
500°C	447.0°C (26.2)	521.7°C (38.6)	549.7°C (20.7)	N/A
575°C	444.8°C (18.3)	530.0°C (22.8)	581.2°C (32.0)	N/A
650°C	427.0°C (9.9)	566.5°C (23.7)	624.4°C (11.6)	293.8°C (1.7)
725°C	419.2°C (3.2)	607.3°C (14.0)	645.7°C (30.6)	372.3°C (5.8)
850°C	514.9°C (8.9)	606.7°C (19.1)	629.6°C (10.5)	403.6°C (12.7)

features in each dTPO curve. For example, the dTPO of carbon obtained from isooctane decomposition at temperatures less than 600 °C contained three superimposed Gaussian peaks I, II, and III. A fourth peak (IV) appeared as a result of isooctane decomposition above 600 °C. This peak shifted to higher oxidation temperature (from 275 °C to 400 °C) as the decomposition temperature increased to 800 °C. TPO of carbon deposited on blank CZO revealed a single oxidation feature at 319 and 392 °C for decompositions at 650 and 800 °C, respectively. No oxidation feature for the 500 °C decomposition sample was observed, due to the low deposited carbon content at that temperature. The Gaussian peak center positions and the total deposited carbon mass fractions associated with each fitted peak are presented in Table 2.2. These values were used to compare the relative amounts of carbon deposited in each feature, and to identify deposited carbon species.

2.4.2.4 Role of decomposition time on the oxidation of carbon deposits

In order to elucidate the formation sequence of carbon species and their morphology, a series of additional short-duration, isothermal isooctane decomposition experiments were performed. The duration of these timed decomposition experiments was chosen to be 2, 10, and 60 minutes. Generally, 2 minutes into isooctane decomposition, catalysts experienced rapid mass gain. After 10 minutes, these same

catalysts experienced much lower carbon deposition rates. Therefore, by limiting isooctane decomposition to 2, 10, and 60 minutes, carbon morphology and oxidation features could be monitored at three stages of the catalyst life: early in carbon growth (at 2 minutes of decomposition), after rapid growth had stopped (10 minutes), and well after rapid growth had stopped (60 minutes). These incremental decomposition experiments were conducted at 500 and 650 °C, because the homogeneous isooctane conversion at these temperatures was less than 100%, leaving some isooctane for catalytic decomposition on the catalyst surface. The dTPO curves for theses incremental decomposition experiments are shown in Fig. 2.7.

For the decomposition at 500 °C, the mass fractions of carbon deposits were 10.3, 85.6, and 86wt% for 2, 10, and 60-minute long decompositions, respectively. Deconvolution of the dTPO curve showed that all three expected TPO features were present in each sample. Within the first 2 minutes, a significant portion of deposited carbon fell within Peak I, located at 440 °C; peaks II and III were located at 499 and 563 °C, respectively. As the decomposition time was increased to 10 minutes, all three dTPO features increased in carbon content but they did not significantly deviate in oxidation peak temperature, save for peak II, which was now centered at 520 °C. Further increasing decomposition time to 60 minutes did not lead to significant changes in the total carbon content (85.5% vs. 86% carbon for 10 and 60-minute decompositions, respectively), however, slight changes in the ratio of carbon content in peaks II and III were observed. Negligible overall mass increase between the 10 and 60-minute decomposition suggests that further carbon was not deposited on the catalyst, and the observed changes in carbon content of peaks II and III were due to restructuring of deposited carbon. The 2, 10, and 60-minute decomposition experiments conducted at 650 °C produced samples with deposited carbon masses of 13.8, 40.3, and 46.8wt%, respectively (Fig. 2.7). A 2-minute decomposition at 650 °C led to three out of the expected four peaks: I, II, and III. These peaks were centered

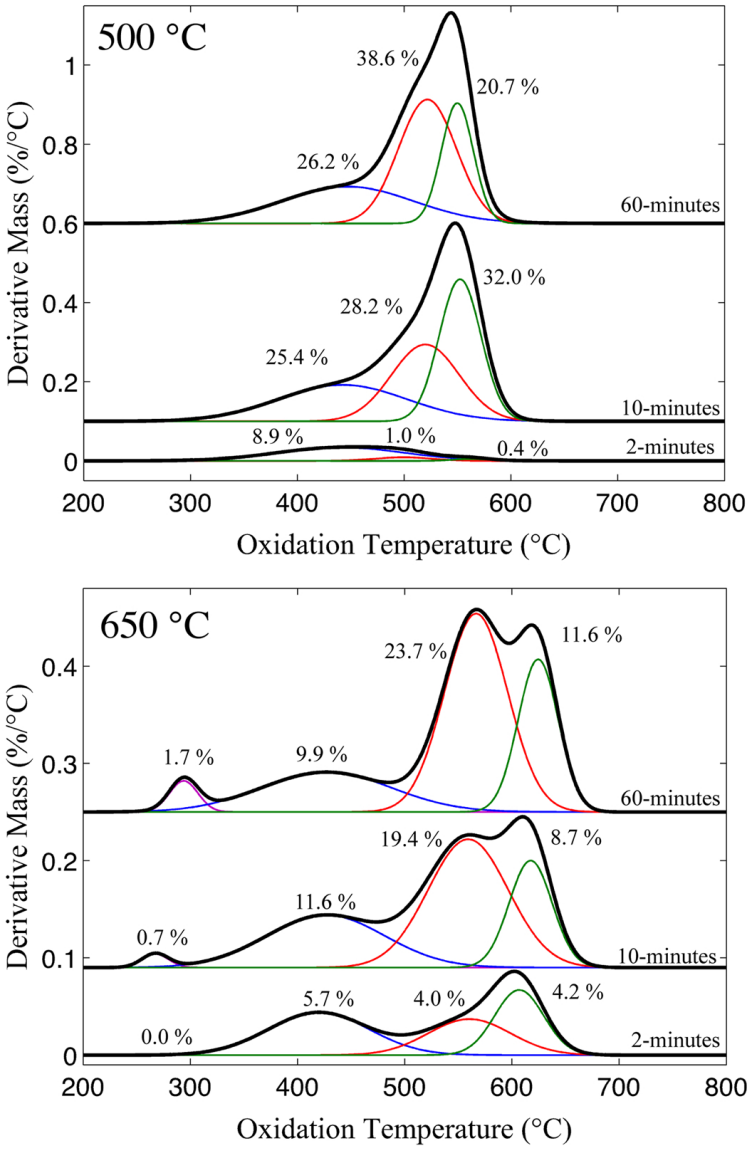

Figure 2.7: Derivative TPO curves for catalysts obtained from timed isooctane decomposition at 500 °C (top) and 650 °C (bottom). Gaussian peaks are labeled with their corresponding carbon weight fraction, as presented in Table 2.

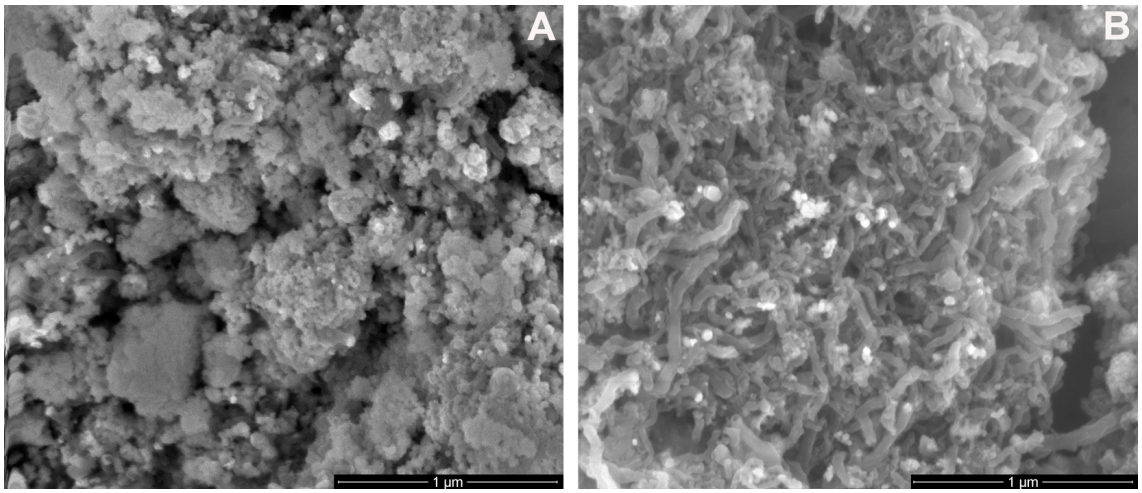

Figure 2.8: Scanning electron micrographs of catalysts post the timed decomposition of isooctane at 500 °C: for 2 minutes (A) and for 10 minutes (B).

at 420, 560, and 607 °C and contained 5.7, 4.0, and 4.2wt% carbon, respectively. 10 minutes into the decomposition, peaks I, II and III increased in carbon content and experienced very slight shifts in peak oxidation temperature. In addition, peak IV appeared in the 10-minute decomposition sample; its peak center was at 267 °C. Further decomposition lead to more carbon content per peak, and a large shift in the position of peak IV to 294 °C.

Fig. 2.8 shows the SEM images of samples from the timed decomposition of isooctane at 500 °C for 2 and 10 minutes. No filamentous carbon was observed within the first 2 minutes of decomposition at 500 °C. 10 minutes into the decomposition, the catalyst appeared to have fully developed filament morphology, as compared to the morphology found in the 60-minute decomposition sample, shown in Fig 2.5A. This result supports the TPO observations presented above.

2.4.2.5 Selective TPO of Carbon Deposits

In order to understand the growth of various carbon morphologies during isooctane decomposition, it was necessary to interrogate each individual dTPO feature

with SEM. However, all deposited carbon samples showed multiple convoluted dTPO features. Samples from isooctane decomposition at 725 °C and 800 °C had minimal overlap in dTPO features. These high-decomposition-temperature samples have two sets of dTPO features that are separated by about 200 °C in oxidation temperature. Therefore, an effort was made to characterize observed dTPO features by selectively oxidizing the carbon that gives rise to the low-temperature dTPO feature while leaving the high-temperature dTPO peaks unaffected. In order to do this, a sample obtained from isooctane decomposition at 725 °C was used, as this sample had clearly separated TPO peaks (at 372 °C and 638 °C). This sample was heated in air at 5 °C min^{-1} to 475 °C to remove the carbon responsible for the TPO peaks at 372 °C. Then the sample was cooled in a N_2 atmosphere to room temperature and then split into two batches: one for SEM characterization, and the other for a standard TPO experiment. This selective TPO procedure worked as intended, as no low temperature peak appeared in the subsequent TPO. Fig. 2.9 shows SEM micrographs of this sample before and after removal of the low temperature TPO features. Both images showed filaments of similar diameter, indicating that these filaments correspond to the high temperature TPO peak. However, there was a significant difference between Fig. 2.9A and 2.9B: namely the appearance of agglomerated particles (either CZO or NiO) entangled with carbon filaments in the partially oxidized sample (Fig. 2.9B). Upon close inspection of Fig. 2.9A, it is plausible to suggest that these particles are present, yet covered by a conductive layer of carbon. It seems unreasonable that the particles observed in Fig. 2.9B migrated along the fibers as a result of low-temperature oxidation.

2.4.3 Role of secondary isooctane decomposition on carbon deposition

The results shown in Fig. 2.3 suggest a correlation between the consumption of isooctane decomposition products and catalyst deactivation due to carbon deposi-

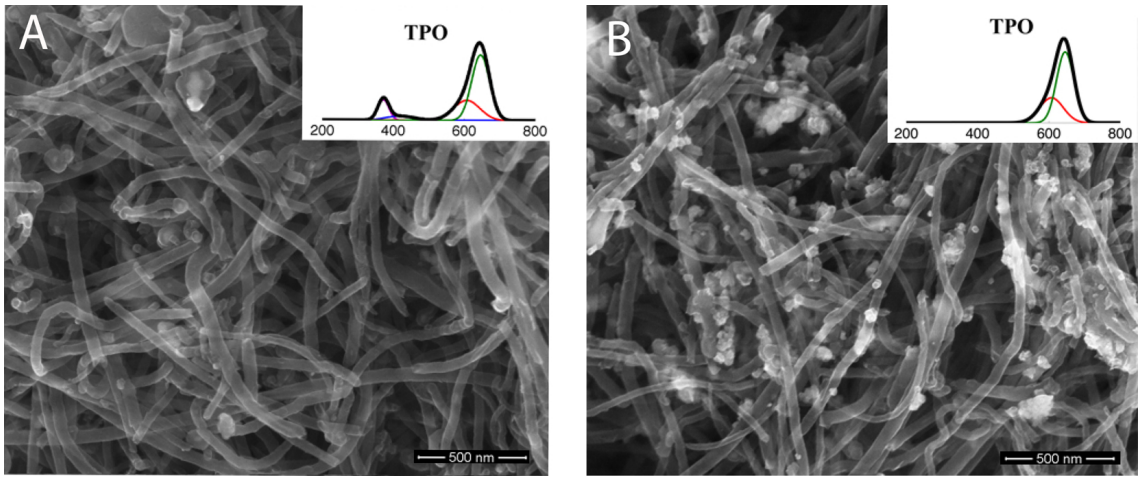

Figure 2.9: SEM micrographs of Ni/CZO catalysts: (A) post isooctane decomposition at 725 °C; (B) after sample A underwent selective TPO that was terminated at 475 °C by removing carbon corresponding to the strong TPO peak IV at 372 °C and the broad and weak TPO peak at 419 °C. Insets are TPO curves for these carbon deposits.

tion. In an effort to assess the role of the intermediate species on carbon deposition, methane and propene catalytic decomposition experiments were conducted. The observed mass changes (normalized to exposed nickel surface area), in addition to the methane and propene IR data (measured during the catalytic experiment) are shown in Fig. 2.10. The low-temperature (500 °C) isooctane and propene decompositions are very similar, as shown in Figs. 2.4 and 2.10. In both cases, the carbon deposition rate is rapid in the first few minutes of the decomposition and relatively slow for the rest of the experiment. In contrast, carbon deposition during the 650 °C methane decomposition experiment shows significant carbon deposition initially and a lower, yet constant, deposition rate for the remainder of the experiment. The carbon deposition behavior of high temperature methane decomposition resembles the deposition of isooctane above 725 °C. This further confirms the hypothesis that carbon deposition at these high temperatures is primarily due to decomposition of secondary species such as methane. It should be pointed out that there was a negative mass change (weight loss of 0.4wt%) during propene decomposition over blank CZO at 500 °C.

IR data recorded maximum concentrations of combustion products (CO, CO_2, and H_2O) 0.4 min after the introduction of isooctane. This indicates the consumption of oxygen stored in CZO by oxidation of propene. Propene decomposition over blank CZO at 700 °C led to a 3.5wt% mass increase due to carbon deposition. Subsequent TPO of this carbon deposit revealed an oxidation peak at 296 °C.

2.5 Discussion

2.5.1 Product distribution of homogeneous isooctane decomposition

The structural complexity of LHCs makes mechanistic studies of carbon deposition from LHCs much more difficult than carbon deposition from methane. Isooctane (2,2,4-trimethypentane) has quaternary, tertiary, secondary, and primary carbon atoms, along with primary, secondary, and tertiary C-H bonds, as shown below:

From the point of view of bond breaking, carbon formation is related not only to the breaking of C-H bonds but also to the breaking of different C-C bonds. Two mechanisms can account for the C-C bond breaking of hydrocarbons: the free radical mechanism that is based on the Rice-Kossiakoff (R-K) theory [74] and the carbonium ion mechanism that deals with catalytic cracking over acidic surfaces of a catalyst [75]. For isooctane, the C-H dissociation energy order is: tertiary C-H (381 kJ/mol) < secondary C-H (397 kJ/mol) < primary C-H (410 kJ/mol) < CH_3-H (435 kJ/mol); while the C-C bond dissociation energy order of isooctane is: quaternary-secondary (C_2-C_3) < tertiary-secondary (C_3-C_4) < primary-quaternary (C_1-C_2) < primary-tertiary (C_4-C_5) where the superscripts refer to the position of a given carbon atom within the molecule as shown above. Applying R-K theory, the main products from isooctane cracking would be isobutene, propylene, and methane. Isobutene production involves the breaking of the C_2-C_3 bond from an isooctane radical at C_2 or C_3 positions, or the secondary cracking of the isooctane radical at C_4 position. The formation of propene

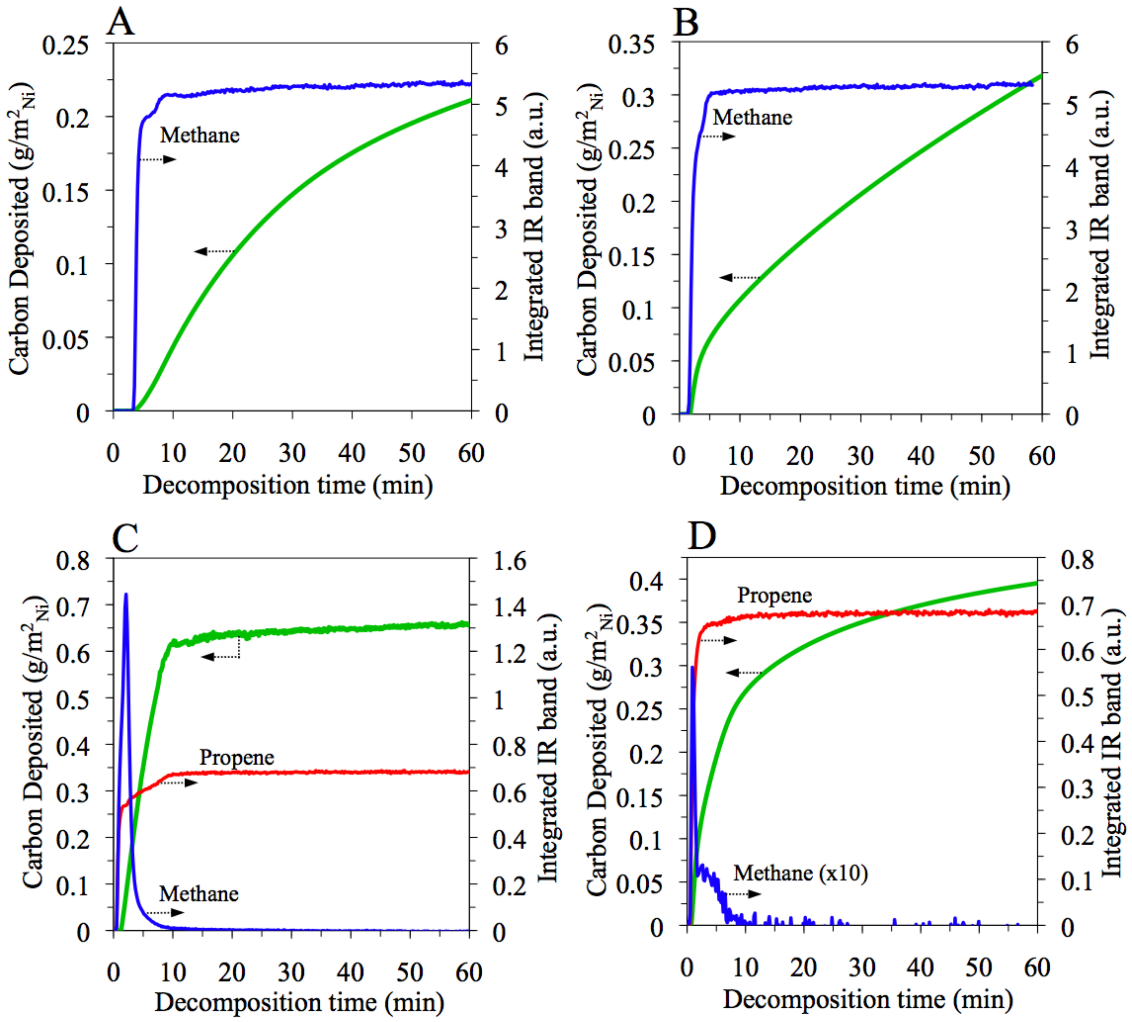

Figure 2.10: Carbon deposition and hydrocarbon IR profiles for the decomposition of methane over Ni/CZO catalyst at 500 °C (A), and 650 °C (B), and propene decomposition over Ni/CZO catalyst at 500 °C (C) and 650 °C (D).

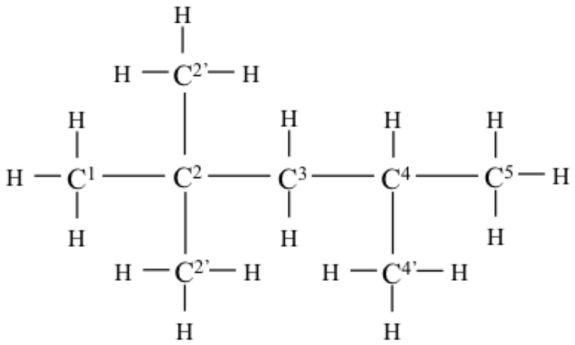

Figure 2.11: Schematic of isooctane, which was used in this study.

stems from the breaking of the C_3-C_4 bond of isooctane radicals, while terminal C-C bond breaking in radicals produces methane. The homogeneous isooctane decomposition product distribution, as shown in Fig. 2.1, obeys the R-K theory. Therefore, the primary product formation sequence for isooctane decomposition as a function of increasing temperature is as follows: isobutene, methane, and propene. As methane is the terminate hydrocarbon product, its maximum concentration was observed at 850 °C in this work.

In previous analysis of homogeneous isooctane thermal decomposition, three main products were found at 680 °C: 59% C_4 (isobutene, 1-butene, and 1,3-butadiene); 19% methane; and 8.5% C_3 (propene, propane) [76]. Another study showed that the initial product distribution from the homogeneous decomposition of 100 mol isooctane at 670 °C included 38 mol H_2, 59 mol methane, 28 mol propene, 115 mol isobutene, and 20 mol C_7H_{14} [77]. In a study at a lower decomposition temperature of 442 °C, four main products (isobutane, isobutene, propene, and methane) were reported [78]. The discrepancy of product distributions reported by different groups can be rationalized based on the difference of reactor configuration, temperature, residence time, and even the analysis method applied. Homogeneous isooctane decomposition products reported in the literature did not include acetylene, benzene, or even ethylene. According to R-K free radical theory, the initial products of isooctane decomposition

should not contain acetylene, ethylene, or benzene. However, these products were detectable in this work at temperatures in excess of 615 °C. Acetylene and ethylene might be derived from further thermal cracking of primary isooctane decomposition products. The formation of these hydrocarbons may be facilitated by longer residence times in the TGA furnace. For example, benzene is known to be one of the major products formed in homogeneous pyrolysis of small hydrocarbons such as ethylene and propene at high temperatures [79, 80].

2.5.2 Catalytic hydrocarbon decomposition and carbon deposition

2.5.2.1 Decomposition products

At low temperatures (500 °C), where the homogeneous decomposition of isooctane was minimal (<3%), the major species consumed catalytically was isooctane (Fig. 2.3). Isooctane consumption coincided with the carbon deposition rate, as evidenced by the DTG curve, indicating that the carbon deposition was a result of catalytic deposition of isooctane into solid carbon and methane. The isooctane consumption and carbon deposition rates reduced to negligible amounts after 15 minutes, which suggests that this carbon buildup led to deactivation of the Ni surface. Catalyst deactivation as it pertains to the catalysts activity toward the decomposition of isooctane can be measured by monitoring the length of time the catalyst is both increasing in mass (depositing carbon) and consuming isooctane (via IR data for isooctane and methane). The general catalytic carbon deposition pathway can be depicted as in Eq. (2.2):

$$Isooctane(iC_8) \rightarrow iC_{8(ads)} \rightarrow C_4H_8, C_3H_6, CH_4 \xrightarrow{\text{catalytic}} C_{(s)} + CH_4 + H_2 \qquad (2.2)$$

At moderately high temperatures (650 °C), isooctane is homogeneously converted (40%) into an array of smaller hydrocarbons, as shown in Fig. 2.1. Catalytically, these

smaller hydrocarbons can also be consumed, producing methane and solid carbon. It appears that the catalyst was active for approximately one third of the amount of time that it was active at 500 °C, based on the full width at half maximum of the DTG peak attributed to carbon deposition. The catalytic consumption curves for isooctane, isobutene, propene, benzene and acetylene coincide with the DTG curve. In addition to the carbon deposition mechanism shown in Eq. (2.2), additional carbon deposition pathways may exist at these elevated temperatures. The homogeneous decomposition of intermediates, such as isobutene and propene, followed by catalytic decomposition of these intermediates may also deposit solid carbon on the catalyst, as schematically illustrated in Eqs. (2.3),(2.4),(2.5),(2.6).

$$iC_8 \xrightarrow{\text{homogeneous}} C_4H_8, C_3H_6, CH_4 \tag{2.3}$$

$$C_4H_8, C_3H_6 \xrightarrow{\text{catalytic}} C_{(s)} + CH_4 + H_2 \tag{2.4}$$

$$C_4H_8, C_3H_6 \xrightarrow{\text{homogeneous}} CH_4 + C_2H_2 + C_2H_4 \xrightarrow{\text{catalytic}} C_{(s)} + CH_4 + H_2 \tag{2.5}$$

$$CH_4 \xrightarrow{\text{catalytic}} C_{(s)} + H_2 \tag{2.6}$$

Based on the results in Fig. 2.1, one would expect that at very high temperatures, e.g. 800 °C, isooctane completely undergoes homogeneous conversion into smaller fragments, such as acetylene and methane, before it reaches the catalyst surface. In fact, even secondary or tertiary decomposition of these fragments occurred homogeneously at these temperatures (Fig. 2.2). Catalysts are active for much shorter times at these very high temperatures (1-3 minutes) and the initial mass of catalytically deposited carbon is relatively small (Fig. 2.3). Equations (2.3) would generally describe carbon deposition at very high temperatures.

2.5.2.2 Classification of Deposited Carbon

Several forms and morphologies of carbon were found to exist under decomposition conditions. In addition to the filaments seen in Figs. 2.5, 2.8, and 2.9, pyrolytic and coating carbon species were also witnessed. In this context, coating carbon is a surface-specific, thin carbon layer, which covers or is dissolved into the surface of the nickel metal, while pyrolytic carbon is surface-insensitive and deposits on all surfaces, such as the mixed oxide support and other carbon deposits.

Pyrolytic carbon deposition was observed during the decomposition of isooctane over blank CZO at 650 and 800 °C. Additionally, surface-insensitive carbon was formed during high-temperature decomposition of propene over blank CZO. The oxidation of these carbon deposits occur coincidentally with the previously identified TPO peak IV (see Fig. 62.6), suggesting that this TPO peak can be attributed to pyrolytic carbon formation. Recall that in the selective oxidation experiment, the carbon filament structures remained, while an apparent conductive over-layer was removed. It can be inferred that the carbon associated with the oxidation peak at 372 °C is pyrolytic, as it uniformly coats the carbon filaments in Fig 9A and the CZO particles in the bare CZO isooctane and propene decomposition experiments.

The presence of a surface-sensitive coating carbon is most noticeable at low decomposition temperatures. During the incremental decomposition of isooctane at 500 °C, 10.3 wt% carbon was deposited in the initial 2 minutes of isooctane decomposition. SEM (Fig. 2.8A) revealed an almost filament-free surface in this sample. However, if a few filaments were formed, these filaments were not large, or numerous enough to account for the 10.3 wt% increase in mass observed. Therefore, the carbon must be uniformly deposited on the surface of the nickel catalyst. Distinction between a surface-sensitive coating carbon and a surface-insensitive pyrolytic carbon is made based on the following three observations: low decomposition temperature, very small concentrations of propene, ethylene, acetylene, and benzene, and the absence

of a dTPO peak between 290 °C and 390 °C. Pyrolytic carbon was never observed during homogeneous hydrocarbon decomposition below 650 °C. The low furnace temperature also led to small conversions of isooctane, and conversely, low concentrations of decomposition products which lead to pyrolytic carbon growth.

Several authors have hypothesized filament growth mechanisms that begin with the diffusion of carbon atoms from the active reforming metal site to the filament nucleation site [39–41]. The observed coating carbon could be associated with this mechanism. However, this classification is based on analysis of carbon deposits formed during low temperature decompositions. More analysis of carbon formed during higher temperature decompositions needs to be conducted to further this hypothesis.

Gaussian peak fitting of the observed dTPO curves (Fig. 2.6) showed that 3 to 4 Gaussian peaks could accurately represent the dTPO curves. By process of elimination, peaks II and III must correspond to the carbon filament structures that are observed in SEM. In the incremental decomposition of isooctane at 500 °C (Fig. 2.7), carbon filaments appeared at 10 and 60 minutes of decomposition (as witnessed via SEM). In addition, the carbon content in peaks II and III increased dramatically over the course of the 60-minute decomposition. Evidence from the selective oxidation experiment (Fig. 2.9) also showed that peaks II and III constitute filament formation. Carbon that was not oxidized in the selective oxidation experiment obviously contained filaments, while the dTPO confirmed the presence of peaks II and III.

2.5.2.3 Effect of secondary decomposition on product distribution and carbon deposition

Methane and propene catalytic decomposition experiments were conducted to further test the hypothesis that homogeneously derived secondary decomposition products were responsible for catalytic carbon deposition during reforming of LHCs. Methane and propene were observed at elevated temperatures from homogeneous

isooctane decomposition. These two species were used to compare catalytic decomposition products and carbon deposition at two decomposition temperatures. Catalyst mass and IR data from low-temperature propene decomposition were very similar to the low-temperature catalytic decomposition of isooctane. Propene decomposition at 500 °C led to a catalyst mass profile that had two distinct regimes: a short initial period of rapid carbon growth, accompanied by the production of methane, followed by a period of much slower growth. As the decomposition temperature increases to 650 °C, the rate of carbon growth at long reaction times also increased, indicating that secondary decomposition products are responsible for carbon deposition at higher temperatures. A similar result was observed during the catalytic decomposition of methane at higher temperatures; carbon deposition at 650 °C mimicked carbon deposition behavior from isooctane catalytic decomposition at higher temperatures ($T \geq 725$ °C), suggesting that the deep decomposition products, like acetylene and methane, also contribute to the deposition of carbon.

2.6 Conclusions

The decomposition of isooctane, which is a representative hydrocarbon for liquid fuels, was investigated over a CZO-supported nickel catalyst using a TGA reactor and FT-IR. The main objective was to gain insight into carbon deposition mechanisms during reforming of liquid hydrocarbons. Results indicate that carbon deposition and hydrocarbon decomposition strongly depend on the reactor temperature. Three different temperature regimes, i.e. $T \leq 575$ °C, 575 °C $< T <$ 725 °C, and $T \geq 725$ °C, were identified with characteristic carbon deposition rates, morphologies, TPO behaviors, and decomposition product distributions. At 500°C, the initial carbon deposition rate was high, and large amounts of carbon accumulated on the catalyst within 13 minutes due to the direct decomposition of isooctane. At moderate temperatures, catalytic decomposition of homogeneously-derived isooctane decompo-

sition products, such as propene, resulted in much faster deactivation of the catalyst due to carbon deposition. In striking contrast, carbon deposition in the high temperature regime (T $\geq$ 725 °C) occurred for a very short period, followed the constant deposition of pyrolytic carbon for the duration of the experiment. TPO and SEM results indicated the presence of four different morphologies and structures of carbon: coating carbon, two types of filamentous carbon, and pyrolytic carbon. The final quantity and deposition rate of these different types of carbon species depended strongly on the decomposition temperature. Primarily, the decomposition temperature dictates the degree of primary hydrocarbon decomposition, which then leads to very specific carbon deposition characteristics.

CHAPTER III

Photocatalytic Reactor Design and Construction

3.1 Abstract

In order to investigate high temperature photocatalytic behaviors, a novel gas-phase photocatalytic reactor was modeled, tested in silico, built, and tested in the laboratory to ensure correct operation. Computer-Aided-Design (CAD) was used extensively to create models of the proposed photocatalytic reactor; this effort aided in the use of computational fluid dynamics (CFD) calculations on the resultant photocatalyst bed. The photocatalytic reactor was specifically designed to maximize the potential of measuring kinetic chemical reaction mechanisms, in order to evaluate high temperature photocatalytic reaction rates.

This work was prompted by unsuccessful attempts to carry out photocatalytic experiments in a traditional down-flow reaction vessel. Experiments in the down-flow arrangement within a vertical tube furnace revealed that the catalyst was light-limited. Therefore, an alternate reaction vessel was required that would allow better illumination of the catalyst in order to measure kinetically relevant photocatalytic reaction rates.

3.2 Photocatalytic Rate Measurement in a Traditional Down-flow Reactor

Preliminary investigation of carbon gasification mechanisms, and photocatalytic enhancement of carbon gasification rates was initially conducted in pursuit of this thesis. Carbon gasification is very endothermic, and requires significant heat input to drive the reaction. Typically, in carbon gasifiers, small amounts of oxygen or air are mixed in the reactant stream to combust a portion of the coal. This partial combustion produces a portion of the heat necessary to drive the gasification reaction. Alternatively, solar thermal energy can be used to produce the required temperatures for carbon gasification, however, due to the high capital costs associated with solar thermal furnaces, this process is not industrially competitive.

In the interest of investigating the utilization of solar energy to drive chemical processes, it was decided to first investigate a photocatalytic catalyst for carbon gasification. For this purpose, a reaction system capable of carbon/coal gasification was built. Figure 3.1 shows the piping diagram used in the design and building of this reactor, while Figure 3.2 shows a photograph of the assembled and working gasification experimental apparatus. The main components are: gas cylinders, mass flow controllers, valves, heated tubing used as a vaporizer, and the furnace/reactor vessel. Reactor inlet and effluent gas analysis can be performed on a Hiden Analytical mass spectrometer. In combination with careful calibrations, the mass spectrometry technique has the ability to accurately quantify the effluent gas composition.

An efficient means of automation was incorporated into the system to allow users to perform simple tasks, such as reduction and oxidation experiments over long, unattended periods. LabView was utilized as a control architecture for the reaction system. By making a few changes to the control program, one can easily make modifications to the experimental procedure. This allows for modifications to the

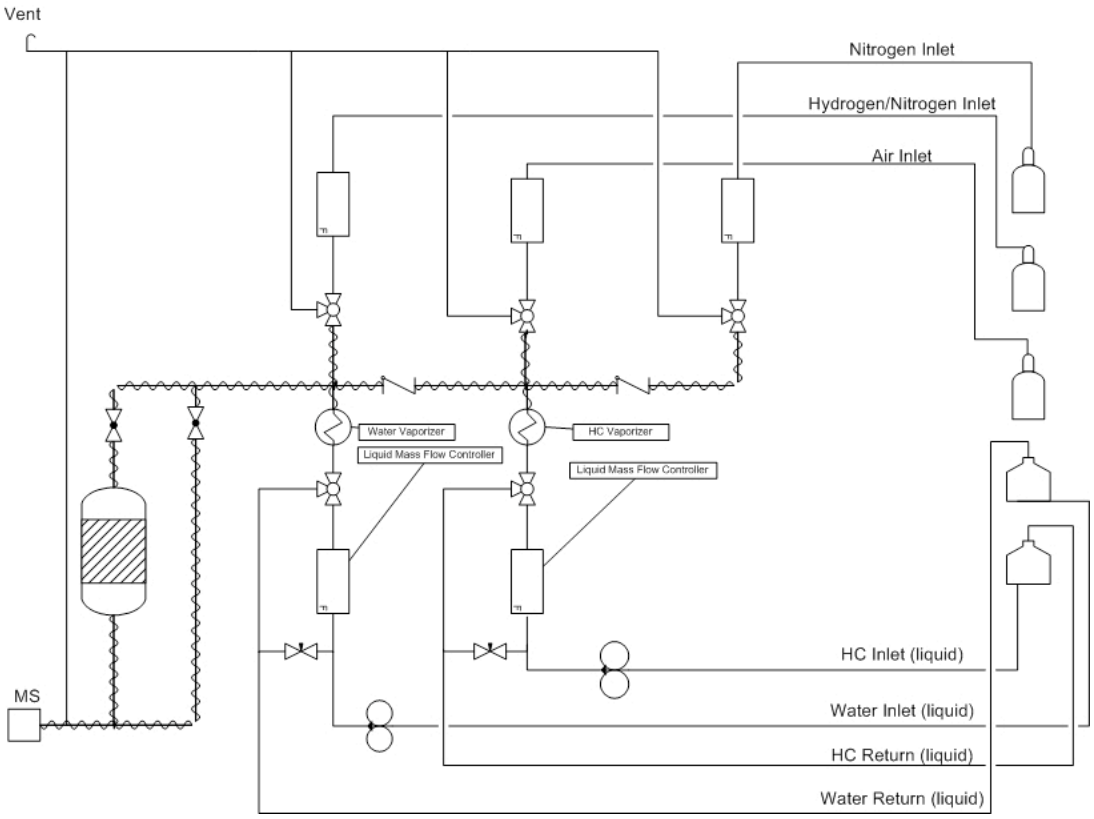

Figure 3.1: Piping & Instrumentation Diagram for gasification reactor.

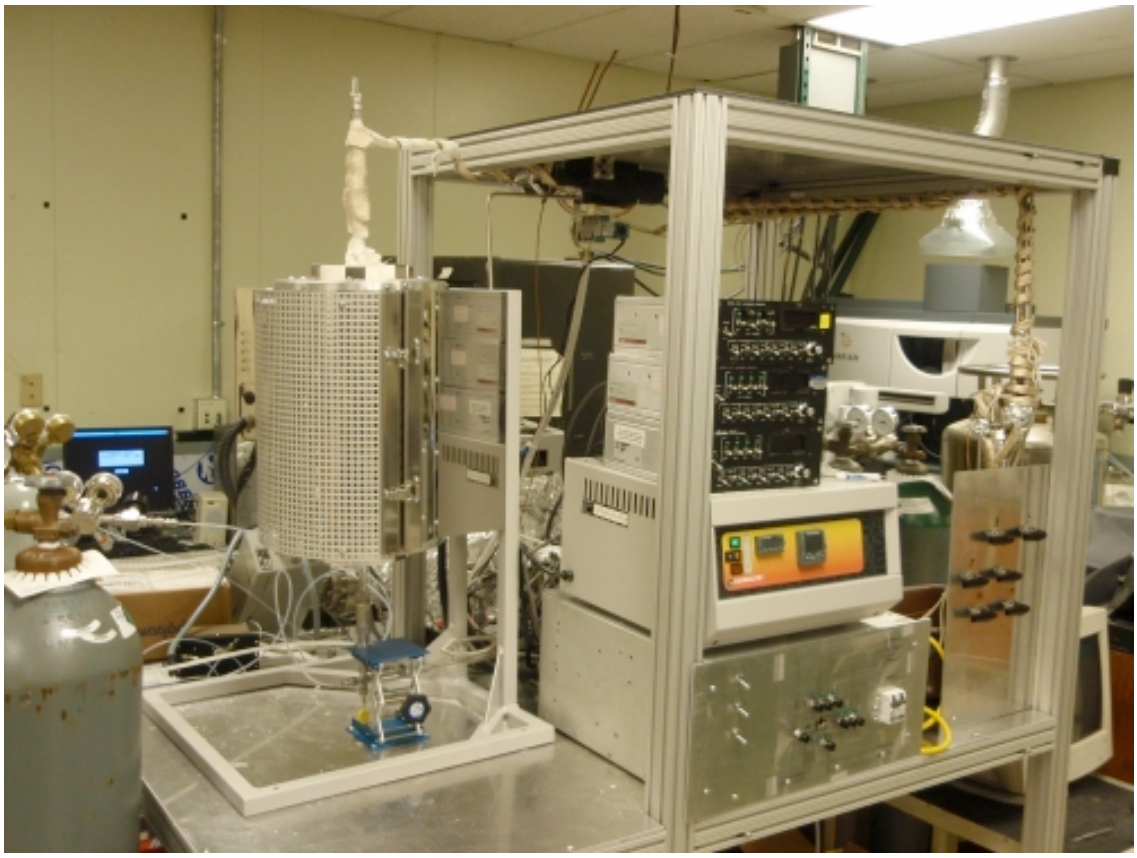

Figure 3.2: Down-flow reaction apparatus, showing vertical tube furnace, mass flow controllers, and a solenoid valve switching control panel.

system via a simple user interface.

In order to control the reactor system electronically, many changes were made to the existing reactor system. For instance, electrically actuated valves (obtained from Swagelok) operated from the digital input/output 5.0VDC lines from a National Instruments Data Acquisition (DAQ) board replaced many of the valves on the original piping diagram.

As reactor support structures and the 1200°C furnace were purchased and assembled for this system, a DAQ board from National Instruments was purchased and installed on a recently bought laboratory PC. This DAQ board has the following pin connections: 4x analogue out (AO), 16x analogue-in (AI), 48x digital in/out (DIO). Although several options for reactor control were possible, it was decided that the valves on the reactor would be controlled via a signal from the DIO. DIO sends a 5VDC control signal to a solid-state relay with a 12VDC power line on the supply side of the SSR. This 12VDC on/off signal then powers a solenoid that, when opened, allows pressurized air to open the reactor valve. With this system in place, a click of the mouse on any password-authorized computer connected to the Internet could potentially open and close a valve on this reaction system.

In an effort to establish the reliability of this reaction system and validate the means of data analysis, it was deemed necessary to reproduce earlier work gasification of activated carbon, as done by Müller et al. As a lab-scale example of solar-thermal gasification, Müller, et al [6]. conducted a series of experiments in which activated carbon samples were irradiated with a mercury arc lamp. This group has researched solar-thermal coal gasification for the past five years, and has experience in simulated solar laboratory experiments. In Müllers experiments, a mercury arc lamp was used as a thermal source, as opposed to a photocatalytic energy source. Activated carbon (Norit Brand) was used to simulate coal and the reactor used was a fluidized bed design. Many experiments were conducted over a range of temperatures with argon

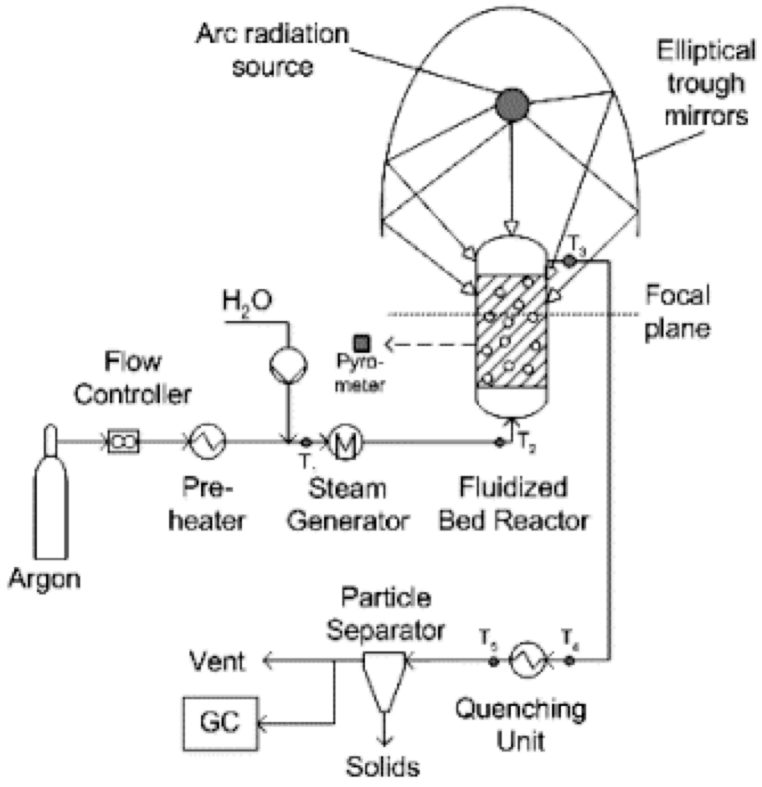

Figure 3.3: Experimental setup for gasification of activated carbon with a solar simulator [6].

to steam molar ratios varying from 8 to 1 (12mol%-50mol% water). Effluent gas was analyzed on a gas chromatograph (GC), which allowed on-stream characterization of hydrogen, carbon monoxide, and carbon dioxide. A schematic of this setup is shown in Figure 3.3.

The results from these experiments were relatively consistent with the theoretical [81] and experimental [82] work done simultaneously by P. Zedwitz, et. al. (a collaborator with A. Steinfeld, a co-author on both papers). Two aspects of this research are notable: use of activated carbon to simulate coal, and use of a concentrated lamp source as heat. If activated carbon can be used as a successful simulator of coal, it is possible to evaluate simplified reaction kinetics and avoid hazardous sulfur and heavy metal compounds.

The experimental procedure at the University of Michigan was very similar to the procedure from Müller, et al. Activated carbon (pellets from Norit) was placed in a quartz reactor tube in the vertical position. This bed was heated to 820°C under argon flow at a heating rate of 10°C/min. Once the temperature and the mass spectrometer data stabilized (usually within 5 minutes of the furnace controller reaching 820°C), 10 minutes of steady state data were collected, followed by the introduction of water flow into the 9 feet long vaporizer tubing fed into the reactor. Water flow remained on at 32 mol% in argon for a period of 75 minutes.

The mass spectrometer collected data at mass/charge values of 2, 15, 28, 40, and 44, corresponding to hydrogen, methane, carbon monoxide, and carbon dioxide, respectively. These data were collected and saved through the LabView control interface in order to allow easy data correlation to temperature data, also recorded using LabView. The mass spectrometer signals were then calibrated to provide a final molar percentage composition of product gases in the effluent stream. Calibrations were done with a 2% certified mixture of hydrogen, carbon monoxide, carbon dioxide, methane, and ethane tank (provided by Cryogenic Gases) mixed to 4 different final concentrations with argon. Each successive mixture was leaked into the vacuum chamber, wherein the mass spectrometer recorded mass/charge signals of these compounds for 5-10 minutes. Each set of data was then fed into an Excel spreadsheet where the differences between the observed and calculated molar percentages of each component were minimized by changing the sensitivity parameters of each component.

Although the thermo-catalytic kinetic reaction rates measured from this reaction were consistent with published values [81], measurement of photo-thermal reaction rates was impossible. The furnace surrounding the down-flow reactor vessel effectively prevented the introduction of ultra-violet light, a requirement when conducting photocatalytic reactions with TiO_2. This lack of photocatalytic activity was confirmed

by methylene blue photocatalytic oxidation experiments.

Methylene blue is a common blue colored dye, which is widely used in the photocatalysis community as a probe molecule for determining photocatalytic oxidation rates, and relative photocatalyst activities [48, 83, 84]. Photo-reactor designs can thereby be tested using a batch-reactor analysis of methylene blue degradation in a mock-experiment. As long as the methylene blue is in the same place (with respect to the UV source) as the photocatalyst bed during gasification, this method should give a measure of the incident UV light. In the present context, the dye-oxidation experiments were conducted to determine the effectiveness of individual photocatalytic reactors. Two reactor configurations were considered (Figure 3.4A). The first reactor (control reactor) was a traditional benchtop system, where the photocatalytic oxidation reaction takes place in an aqueous suspension consisting of 500 micromolar methylene blue in deionized water and approximately 100mg Degussa P25 TiO_2 per liter of solution. The second reactor was arranged to occupy the same dimensions as the steam reforming/gasification catalyst within the tube furnace, and contained the same dye/TiO_2/water solution as the benchtop configuration.

Results from this experiment can be seen in Figure 3.4B, which shows the normalized concentration of methylene blue dye as a function of reaction time. In this batch reaction system, the measure of improved photocatalytic reaction is the observation of a steep drop in dye concentration as a function of time. In this experiment, the photocatalytic reaction vessel in the tubular furnace was indeed a poorly performing photocatalytic reaction vessel.

Therefore, since it proved impractical to measure photocatalytic reaction rates within this furnace, a new approach was required to introduce both heat and light to the photocatalyst bed in order to study elevated temperature photocatalytic rates.

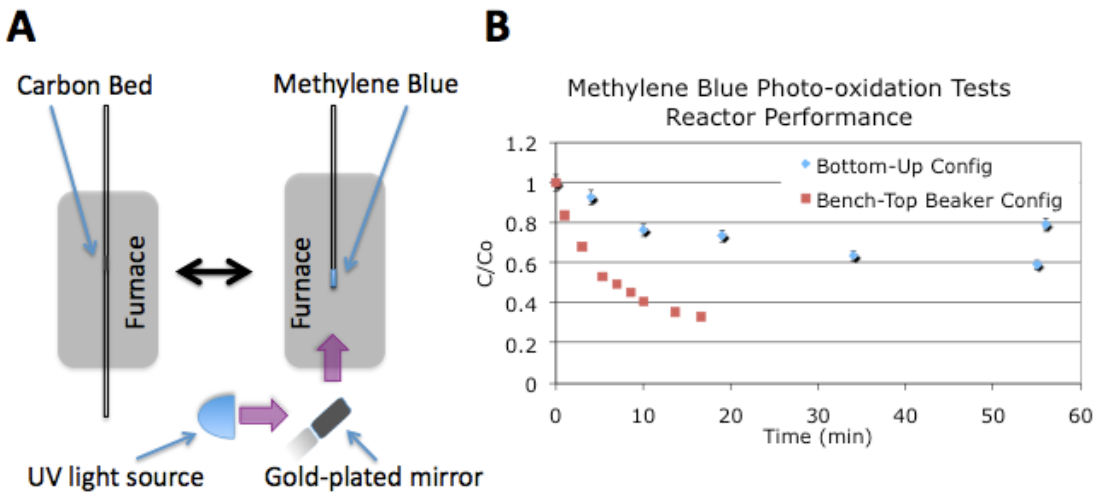

Figure 3.4: Illustration of the arrangement of the catalyst within the down flow tube furnace and the placement of methylene blue during a test photocatalytic experiment (A). Also shown is the normalized methylene blue concentration during the experiment shown in (A) as well as during an experiment on the bench top, where UV illumination is not rate limiting (B).

3.3 Photocatalyst Reactor Design Constraints

The investigation of photocatalytic enhancement of the coal gasification reaction illustrated the necessity for a specifically designed photocatalytic reaction vessel, capable of the measurement of kinetically limited rates of photocatalytic reactions. In addition to the constraint of light introduction to the catalyst bed, a perfect chemical reactor would have a uniform temperature distribution profile across the catalyst bed and a uniform gas flow profile across the catalyst bed. Therefore, in designing a new photocatalytic reactor, an attempt was made to capture a qualitative understanding of both temperature and gas flow distributions.

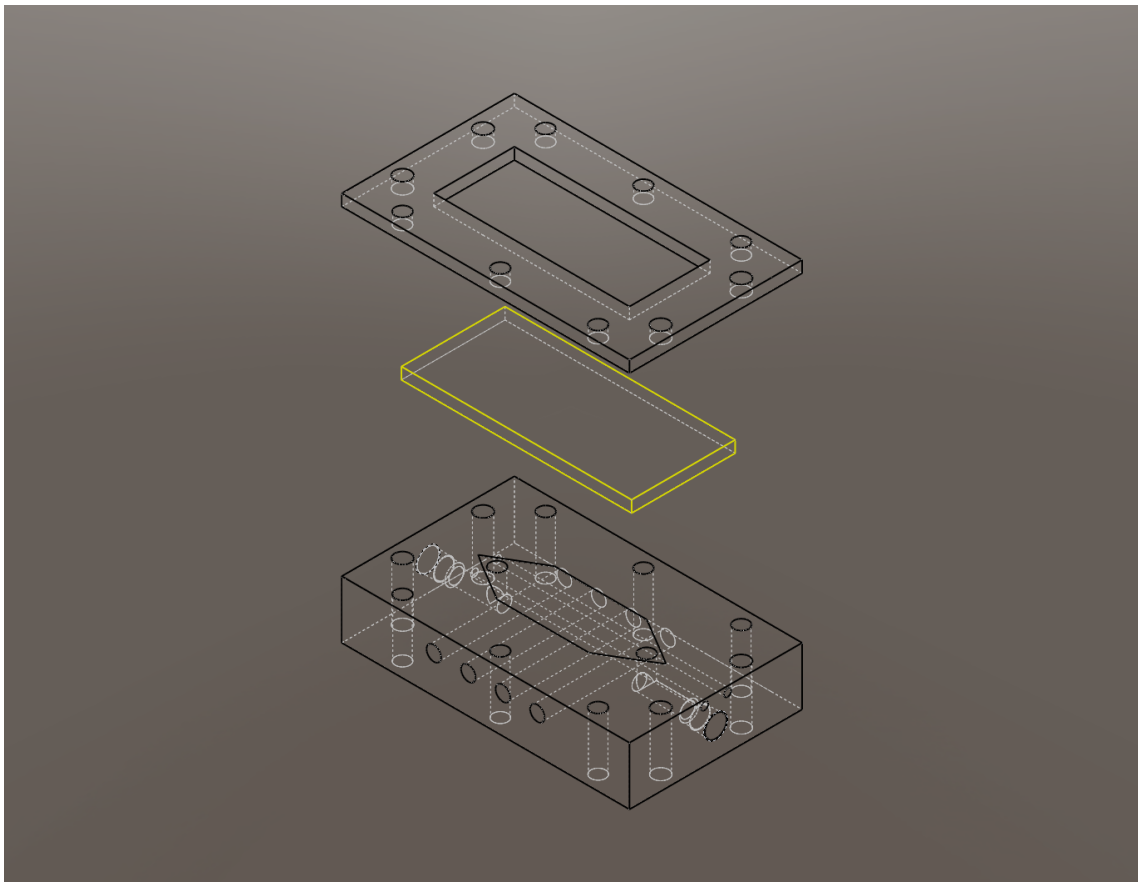

Figure 3.5: SolidWorks model of photocatalytic reactor, with the base (bottom), quartz catalyst cover (middle, outlined in yellow), and compression plate (top).

3.4 Computer Aided Design and Computational Fluid Dynamics Modeling of Photocatalytic Reactor

A model of the photocatalytic reactor used for oxidation experiments was designed in SolidWorks (Figure 3.5) and tested for uniform temperature distributions and gas flow distributions across the catalyst bed using COMSOL Multiphysics simulations (Figures 3.6, and 3.7, respectively). The simulation demonstrated sufficient uniformity in both temperature and gas velocity profiles across the catalyst bed.

The concept photocatalytic reactor was designed to have one large base-plate, which contains a depression for the placement of photocatalyst, thermocouple through-